ANNALS OF GEOPHYSICS, 65, 4, PE426, 2022; doi:10.4401/ag-8570
OPEN ACCESS

3-D data-space joint inversion of gravity and magnetic data using a correlation-analysis constraint

Sheng Liu[1,2,3], Shuanggen Jin[*,3,4,5], Songbai Xuan[3], Xiang Liu[1]

(1) Xinjiang Astronomical Observatory, Chinese Academy of Sciences, Urumqi 830011, China
(2) University of Chinese Academy of Sciences, Beijing 100049, China
(3) Shanghai Astronomical Observatory, Chinese Academy of Sciences, Shanghai 200030, China
(4) School of Surveying and Land Information Engineering, Henan Polytechnic University, Jiaozuo 454000, China
(5) Zhuhai Fundan Innovation Institute, Creative Valley, Hengqin New District, Zhuhai 518057, China

Article history: received November 9, 2021; accepted March 30, 2022

Abstract

Non-uniqueness, low computational efficiency and large memory requirements are main issues for geophysical data inversion. In this paper, we propose an efficient algorithm for 3D correlation-analysis joint inversion of gravity and magnetic data with high accuracy and low computation effort. Firstly, since the number of the observed field data is smaller than the number of inverted parameters, the calculations of the correlation-analysis for joint inversion of gravity and magnetic data in model space (MS) are transformed into the equivalent calculations in data space (DS), which can reduce the dimensions of the calculation domain, improve the computation efficiency and reduce the non-uniqueness. Then, an improved conjugate gradient (ICG) method is employed for the optimization algorithm, which can facilitate the use of stable functions with sparse factors and improve the accuracy of the inversion. The inversion performed by the combined DS-ICG method for synthetic data tests shows the calculation effort can be effectively reduced, and the issues with non-uniqueness are improved. Finally, the test by real field data can delineate the distribution of underground geological bodies, which illustrates the strong stability and good applicability of our extended method.

Keywords: Joint inversion of gravity and magnetic data; Model-space (MS); Data-space (DS); Correlation-analysis constraint; Improved conjugate gradient (ICG)

1. Introduction

Different geophysical models can reproduce given observations with the same degree of accuracy, and any chosen model can be significantly different than the true generating source. To reduce this ambiguity, prior information is commonly introduced in the inversion [e.g., Farquharson et al., 2008; Lelièvre, 2009; Caratori Tontini et al., 2006; Li and Oldenburg, 2000b] and/or multiple independent geophysical data are used for a joint inversion [e.g., Afnimar

and Nakagawa, 2002; Bosch, 1999; Bosch and Mc Gaughey, 2001; Gallardo and Meju, 2003, 2004; Lelièvre et al., 2012; Moorkamp et al., 2011]. Currently, there are different types of proposed joint inversion methods. The first type assumes that multiple geophysical data correspond to the same physical property model. [e.g., Guo, et al., 2009; Geng et al., 2014; Qin et al., 2016; Zhdanov and Lin, 2017; Hou et al., 2019; Fu et al., 2016; Vozoff and Jupp, 1975]. The second type involves joint inversion methods based on statistical or empirical petrophysical relationships [e.g., Gardner et al., 1974; Lines et al., 1988; Sun and Li, 2015, 2016]. Other joint inversion methods are based on different physical property models with similar spatial distribution structures, such as cross-gradient joint inversion [e.g., Haber and Oldenburg, 1997; Gallardo and Meju, 2003; Fregoso and Gallardo, 2009; Vatankhah et al., 2022], correlation-analysis joint inversion [e.g., Oldenburg and Li, 1999; Lelièvre et al., 2012; Yin et al., 2018; Gao et al., 2019], and the joint inversion based on Gramian constraint [e.g., Zhdanov et al., 2012; Lin and Zhdanov, 2018]. In this case, the non-uniqueness can be effectively reduced by properly combining the correlation-analysis constraint with the joint inversion [e.g., Yin et al., 2018; Gao et al., 2019].

Generally, the joint inversion is always performed in the MS. As the volume cells continue to increase, the computation cost also increases substantially. The DS method [Siripunvarapor et al., 2005a] can convert the calculations in MS to the calculations in DS. Since the number of field data is less than the number of the grid cells, the cross-gradient inversion in the DS requires less computation cost and improves the inversion accuracy [e.g., Pak, Li and Kim, 2017; Zhang et al., 2020; Zhang et al., 2022]. In this paper, the correlation-analysis joint inversion of gravity and magnetic data is extended to the DS for reducing the computation cost and improving the inversion accuracy.

Many optimization algorithms have been adopted in geophysical inversion, such as the Gauss-Newton (GN) method [e.g., Gallardo and Meju, 2004; Gallardo et al., 2012], the quasi-Newton method [e.g., Moorkamp et al., 2011] and the conjugate gradient (CG) method. [e.g., Moorkamp et al., 2011; Zhdanov et al., 2012]. The CG method only needs to calculate the products of Jacobian matrix for arbitrary vectors, instead of performing the full multiplication of the Jacobian matrix. Therefore, the CG method is instrumental for large-scale calculation and widely used for 3D inversion of field data. However, the CG method needs to continuously calculate many small iterative steps during the inversion process, which requires long execution times. The ICG method by combining the inner and outer loop iteration has been successfully used for the joint inversion of gravity and gravity gradient data [e.g., Zhang et al., 2021], reducing the number of iterations and increasing the convergence speed.

In this paper, we extend the correlation-analysis joint inversion of gravity and magnetic data to the DS computation, which can reduce the dimensions of the calculation domain and improve the computation efficiency. Then, the ICG method is introduced to reduce the number of iterations and increase the convergence speed. Finally, the accuracy and advantages of the DS-ICG joint inversion method are verified by synthetic data and real field data tests.

2. Methodology

2.1 Objective functions for joint inversion

The two physical parameters related to gravity and magnetic data are density $\boldsymbol{m}_1$ and magnetization $\boldsymbol{m}_2$. Objective functions of the correlation-analysis joint inversion of gravity and magnetic data are represented as

$$\begin{aligned}\phi_1 &= \phi_{\mathrm{d}}^1 + \lambda_1\phi_m^1 + \mu_1\phi_{\mathrm{cor}}^1 \\ &= \|\boldsymbol{d}_1 - \boldsymbol{G}_1\boldsymbol{m}_1\|_2^2 + \lambda_1\left\|\boldsymbol{w}_1\left(\boldsymbol{m}_1 - \boldsymbol{m}_1^{\mathrm{ref}}\right)\right\|_2^2 + \mu_1[|\boldsymbol{R}|^2|\boldsymbol{S}|^2 - (\boldsymbol{R}\cdot\boldsymbol{S})^2]\end{aligned}, \tag{1}$$

$$\begin{aligned}\phi_2 &= \phi_{\mathrm{d}}^2 + \lambda_2\phi_m^2 + \mu_2\phi_{\mathrm{cor}}^2 \\ &= \|\boldsymbol{d}_2 - \boldsymbol{G}_2\boldsymbol{m}_2\|_2^2 + \lambda_2\left\|\boldsymbol{w}_2\left(\boldsymbol{m}_2 - \boldsymbol{m}_2^{\mathrm{ref}}\right)\right\|_2^2 + \mu_2[|\boldsymbol{R}|^2|\boldsymbol{S}|^2 - (\boldsymbol{R}\cdot\mathbf{S})^2]\end{aligned}, \tag{2}$$

where

- ϕ_1 represents the objective function of gravity data;
- ϕ_{d}^1 represents the data misfitting of gravity data;

- ϕ_m^1 represents the stable function of gravity data;
- ϕ_{cor}^1 represents the correlation-analysis constraint of gravity data;
- $\boldsymbol{d}_1$ represents the observed gravity data;
- $\boldsymbol{m}_1^{\text{ref}}$ represents the reference density model;
- $\boldsymbol{G}_1$ represents the forward response of the density model;
- $\boldsymbol{w}_1$ represents the weighting matrix of the density model;
- λ_1 represents the regularization parameter of gravity data;
- μ_1 represents the weighting parameter of the correlation-analysis constraint of gravity data;
- ϕ_2 represents the objective function of magnetic data;
- ϕ_{d}^2 represents the data misfitting of magnetic data;
- ϕ_m^2 represents the stable function of magnetic data;
- ϕ_{cor}^2 represents the correlation-analysis constraint of magnetic data;
- $\boldsymbol{d}_2$ represents the observed magnetic data;
- $\boldsymbol{m}_2^{\text{ref}}$ represents the reference magnetization model;
- $\boldsymbol{G}_2$ represents the forward response of the magnetization model;
- $\boldsymbol{w}_2$ represents the weighting matrix of the magnetization model;
- λ_2 represents the regularization parameter of magnetic data;
- μ_2 represents the weighting parameter of the correlation-analysis constraint of magnetic data;
- $\boldsymbol{R} = \left(\boldsymbol{m}_1^2 - \overline{\boldsymbol{m}_1^2}\right)$ and $\boldsymbol{S} = \left(\boldsymbol{m}_2^2 - \overline{\boldsymbol{m}_2^2}\right)$.

We also introduce $\overline{\boldsymbol{m}_1^2} = \frac{1}{\mathrm{N}}\sum_{\mathrm{i}=1}^{\mathrm{N}} \boldsymbol{m}_{1\mathrm{i}}^2$, $\overline{\boldsymbol{m}_2^2} = \frac{1}{\mathrm{N}}\sum_{\mathrm{i}=1}^{\mathrm{N}} \boldsymbol{m}_{2\mathrm{i}}^2$, respectively, and N is the number of the volume pixels. Because of the strong constraint ability of the correlation-analysis constraints [e.g., Gao et al. 2019], μ_1 and μ_2 are set to small positive values, respectively. The correlation-analysis constraint calculates the square of the physical property model parameters minus the mean of the square of the physical property model parameters to describe the spatial distribution of the physical property model. Furthermore, structural coupling is achieved by calculating the sinusoidal correlation of the spatial distributions of different physical property models. Stronger correlation between the spatial distribution of density model and the spatial distribution of magnetization model induces smaller values of the correlation-analysis constraints.

The regularization method of elastic nets [Zhang and Li., 2019] can avoid excessive sharp boundaries of the recovered models obtained by L1-norm regularization technology and improve excessive smooth boundaries of the recovered models obtained by L2-norm regularization technology. For these reasons we adopt the elastic-nets regularization method in this paper. For the convenience of computation, we modify the smooth constraint in the stable function of the elastic-nets as follows

$$\begin{aligned}\phi_{m_1} &= (1-\tau_1)\phi_{m_{1_{\mathrm{L1}}}} + \tau_1\phi_{m_{1_{\mathrm{L2}}}}(\boldsymbol{m}_1) \\ &= (1-\tau_1)\|\boldsymbol{m}_1\|_1^1 + \tau_1\|\boldsymbol{m}_1\|_2^2 = \left|\boldsymbol{w}_{m_1}\boldsymbol{m}_1\right|_2^2\end{aligned}, \tag{3}$$

where

$$\boldsymbol{w}_{\boldsymbol{m}_1} = \left(\frac{\partial\phi_{m_1}}{\partial\boldsymbol{m}_1}/\boldsymbol{m}_1\right)^{1/2} = \left[(1-\tau_1)\left(\boldsymbol{m}_1^2+\varepsilon^2\right)^{(-1/2)} + \tau_1\boldsymbol{I}\right]^{1/2}, \tag{4}$$

and τ_1 represents a non-negative weight factor (τ_1 is in the range of 0-1). $\phi_{m_{1_{\mathrm{L1}}}}$ and $\phi_{m_{1_{\mathrm{L2}}}}$ are the L1-norm regularization term and the L2-norm regularization term, respectively, and $\boldsymbol{w}_{m_1}$ is the weighting matrix of density model. $\boldsymbol{w}_1$ is the result of multiplying $\boldsymbol{w}_{m_1}$ by depth weighting matrix [Li and Oldenburg., 1996, 2000b], ε is sparsity factor and $\boldsymbol{I}$ is identity matrix. For the magnetization model $\boldsymbol{m}_2$, the stable function and other weighting matrices agree with the corresponding parts of the density model $\boldsymbol{m}_1$.

2.2 The MS-ICG joint inversion method

The most common optimization algorithms adopted in geophysical inversion are least square method, Newton method, GN method and CG method. When performing inversion by the GN method, the stable function without a sparse factor is always adopted, while the regularization factor is always obtained by the L-curve method [e.g., Tikhonov and Arsenin, 1977]. In this paper, the stable function, i.e., the minimum difference between the recovered model and the reference model, is used for the joint inversion, and the corresponding solution process of the correlation-analysis joint inversion based on the GN method is shown in Algorithm 1 (Appendix A). Currently, more regularization techniques include a sparsity factor, which requires a re-weighting process during the inversion process. Furthermore, the adaptive regularization parameter method is generally adopted [Portniaguine et al., 1999]. The ICG method [Zhang et al., 2021] facilitates field data inversion using stable function with sparse factors. Additionally, the ICG method has the same advantages of the CG method, with small memory cost and fast convergence. Therefore, in this paper, the ICG method and the stable function with a sparse factor are adopted for the correlation-analysis joint inversion. Furthermore, the adaptive regularized parameter method is also adopted. Firstly, a suitable λ_0 is selected and the calculations for subsequent regularization parameters are represented as

$$\lambda_{k+1} = \lambda_k q, \tag{5}$$

where q is the scale factor, and the range of q is set to $0 \sim 1.0$.

The ICG method [Zhang et al., 2021] is improved on the basis of the GN method and the CG method, and its core depends on the inner loop and the outer loop. The outer loop is used to initialize and prepare the matrices required for the subsequent calculations, etc., and the inner loop is used to calculate the model update. Firstly, the expression of the model update of the k-th iteration based on the GN method is given by

$$\Delta \boldsymbol{m}_1 = \boldsymbol{m}_1^k - \boldsymbol{m}_1^{k-1} = -\boldsymbol{H}_{1,k}^{-1} \boldsymbol{g}_1^k, \tag{6}$$

where $\Delta \boldsymbol{m}_1$ is the model update of the density model, and the other matrices are represented as

$$\boldsymbol{H}_{1,k} = \boldsymbol{G}_1^T \boldsymbol{G}_1 + \lambda_{1,k} \boldsymbol{w}_{1,k}^T \boldsymbol{w}_{1,k} + 2\mu_1 \frac{N-1}{N} \mathrm{diag}\left[\left| \boldsymbol{S}_{1,k} \right|^2 \boldsymbol{R}_{1,k} - \left(\boldsymbol{R}_{1,k} \cdot \boldsymbol{S}_{1,k} \right) \boldsymbol{S}_{1,k} \right], \tag{7}$$

$$\boldsymbol{g}_1^k = -\boldsymbol{G}_1^T \left(\boldsymbol{d}_1 - \boldsymbol{G}_1 \boldsymbol{m}_1^{k-1} \right) + \lambda_{1,k} \left(\boldsymbol{m}_1^{k-1} - \boldsymbol{m}_1^{ref} \right) + 2\mu_1 \frac{N-1}{N} \mathrm{diag}\left[\left| \boldsymbol{S}_{1,k} \right|^2 \boldsymbol{R}_{1,k} - \left(\boldsymbol{R}_{1,k} \cdot \boldsymbol{S}_{1,k} \right) \boldsymbol{S}_{1,k} \right] \boldsymbol{m}_1^{k-1}. \tag{8}$$

In Eq. (8), $\boldsymbol{m}_1^{k-1}$ is used as the reference model for the k-th iteration. Therefore, $\boldsymbol{g}_1^k$ in Eq. (8) can be transformed into the following form.

$$\boldsymbol{g}_1^k = -\boldsymbol{G}_1^T \left(\boldsymbol{d}_1 - \boldsymbol{G}_1 \boldsymbol{m}_1^{k-1} \right) + 2\mu_1 \frac{N-1}{N} \mathrm{diag}\left[\left| \boldsymbol{S}_{1,k} \right|^2 \boldsymbol{R}_{1,k} - \left(\boldsymbol{R}_{1,k} \cdot \boldsymbol{S}_{1,k} \right) \boldsymbol{S}_{1,k} \right] \boldsymbol{m}_1^{k-1} \tag{9}$$

In Eq. (7), let $\boldsymbol{C}_{1,k} = \left\{ \lambda_{1,k} \boldsymbol{w}_{1,k}^T \boldsymbol{w}_{1,k} + 2\mu_1 \frac{N-1}{N} \mathrm{diag}\left[\left| \boldsymbol{S}_{1,k} \right|^2 \boldsymbol{R}_{1,k} - \left(\boldsymbol{R}_{1,k} \cdot \boldsymbol{S}_{1,k} \right) \boldsymbol{S}_{1,k} \right] \right\}^{-1}$ and $\widehat{\boldsymbol{d}}_1^k = \boldsymbol{d}_1 - \boldsymbol{G}_1 \boldsymbol{m}_1^{k-1}$. $\boldsymbol{C}_{1,k}$ is a $N \times N$-dimensional invertible diagonal matrix. $\widehat{\boldsymbol{d}}_1$ is a M-dimensional vector and M is the number of field data. Generally, the number N is much larger than the number M. Therefore, Eq. (6) can be transformed into the following form,

$$\Delta \boldsymbol{m}_1 = \left\{ \boldsymbol{G}_1^T \boldsymbol{G}_1 + \boldsymbol{C}_{1,k}^{-1} \right\}^{-1} \left\{ \boldsymbol{G}_1^T \widehat{\boldsymbol{d}}_1^k - 2\mu_1 \frac{N-1}{N} \mathrm{diag}\left[\left| \boldsymbol{S}_{1,k} \right|^2 \boldsymbol{R}_{1,k} - \left(\boldsymbol{R}_{1,k} \cdot \boldsymbol{S}_{1,k} \right) \boldsymbol{S}_{1,k} \right] \boldsymbol{m}_1^{k-1} \right\}, \tag{10}$$

where $\boldsymbol{G}_1^{\mathrm{T}}\boldsymbol{G}_1+\boldsymbol{C}_{1,\mathrm{k}}^{-1}$ is a N × N-dimensional matrix and $\left\{\boldsymbol{G}_1^{\mathrm{T}}\widehat{\boldsymbol{d}}_1^{k}-2\mu_1\frac{\mathrm{N}-1}{\mathrm{N}}\mathrm{diag}\left[\left|\boldsymbol{S}_{1,\mathrm{k}}\right|^2\boldsymbol{R}_{1,\mathrm{k}}-\left(\boldsymbol{R}_{1,\mathrm{k}}\cdot\boldsymbol{S}_{1,\mathrm{k}}\right)\boldsymbol{S}_{1,\mathrm{k}}\right]\boldsymbol{m}_1^{\mathrm{k}-1}\right\}$ is a N-dimensional vector. In addition, the model update equation of the magnetization model is similar to the model update equation of the density model in Eq. (10). The detailed process of the MS-ICG joint inversion in this paper is shown in Algorithm 2 (Appendix B).

2.3 The DS-ICG joint inversion method

The DS method [Siripunvaraporn and Egbert 2000; Siripunvaraporn et al. 2005a] can convert the computations in the MS to the computations in the DS through matrices transformations. Since the number N of the volume pixels is much larger than the number M of field data, the calculations in the MS require solving a N × N-dimensional equation, while the calculations in the DS only need to solve a M × M-dimensional equation. Therefore, the DS method adopted for inversion can effectively reduce the computation cost [Pilkington 2009; Zhang et al., 2020; Zhang et al. 2022]. In this paper, the DS method is applied to the correlation-analysis inversion of gravity and magnetic data and the model update (Eq. (10)) in the MS is transformed into the model update in the DS as the following formula.

$$
\begin{aligned}
\Delta\boldsymbol{m}_1 &= \left(\boldsymbol{G}_1^{\mathrm{T}}\boldsymbol{G}_1+\boldsymbol{C}_{1\mathrm{k}}^{-1}\right)^{-1}\left\{\boldsymbol{G}_1^{\mathrm{T}}\widehat{\boldsymbol{d}}_1^{\mathrm{k}}-2\mu_1\frac{\mathrm{N}-1}{\mathrm{N}}\mathrm{diag}\left[\left|\boldsymbol{S}_{1,\mathrm{k}}\right|^2\boldsymbol{R}_{1,\mathrm{k}}-\left(\boldsymbol{R}_{1,\mathrm{k}}\cdot\boldsymbol{S}_{1,\mathrm{k}}\right)\boldsymbol{S}_{1,\mathrm{k}}\right]\boldsymbol{m}_1^{\mathrm{k}-1}\right\} \\
&= \boldsymbol{C}_{1,\mathrm{k}}\left(\boldsymbol{G}_1^{\mathrm{T}}\boldsymbol{G}_1\boldsymbol{C}_{1,\mathrm{k}}+\mathrm{I}\right)^{-1}\left(\boldsymbol{G}_1^{-\mathrm{T}}\right)^{-1}\widehat{\boldsymbol{d}}_1^{\mathrm{k}} \\
&\quad -2\mu_1\frac{\mathrm{N}-1}{N}\boldsymbol{C}_{1,\mathrm{k}}\left(\boldsymbol{G}_1^{\mathrm{T}}\boldsymbol{G}_1\boldsymbol{C}_{1,\mathrm{k}}+\boldsymbol{I}\right)^{-1}\left\{\mathrm{diag}\left[\left|\boldsymbol{S}_{1,\mathrm{k}}\right|^2\boldsymbol{R}_{1,\mathrm{k}}-\left(\boldsymbol{R}_{1,\mathrm{k}}\cdot\boldsymbol{S}_{1,\mathrm{k}}\right)\boldsymbol{S}_{1,\mathrm{k}}\right]\boldsymbol{m}_1^{\mathrm{k}-1}\right\} \\
&= \boldsymbol{C}_{1,k}\left[\boldsymbol{G}_1^{-\mathrm{T}}\left(\boldsymbol{G}_1^{T}\boldsymbol{G}_1\mathrm{C}_{1,k}+\mathrm{I}\right)\right]^{-1}\widehat{\boldsymbol{d}}_1^{k} \\
&\quad -2\mu_1\frac{\mathrm{N}-1}{\mathrm{N}}\mathrm{C}_{1,\mathrm{k}}\left(\boldsymbol{G}_1^{\mathrm{T}}\boldsymbol{G}_1\boldsymbol{C}_{1,\mathrm{k}}+\boldsymbol{I}\right)^{-1}\left\{\mathrm{diag}\left[\left|\boldsymbol{S}_{1,\mathrm{k}}\right|^2\boldsymbol{R}_{1,\mathrm{k}}-\left(\boldsymbol{R}_{1,\mathrm{k}}\cdot\boldsymbol{S}_{1,\mathrm{k}}\right)\boldsymbol{S}_{1,\mathrm{k}}\right]\boldsymbol{m}_1^{\mathrm{k}-1}\right\} \\
&= \boldsymbol{C}_{1,\mathrm{k}}\boldsymbol{G}_1^{\mathrm{T}}\left(\boldsymbol{G}_1\boldsymbol{C}_{1,\mathrm{k}}\boldsymbol{G}_1^{\mathrm{T}}+\boldsymbol{I}\right)^{-1}\widehat{\boldsymbol{d}}_1^{\mathrm{k}} \\
&\quad -2\mu_1\frac{\mathrm{N}-1}{\mathrm{N}}\left[\boldsymbol{I}-\boldsymbol{C}_{1,\mathrm{k}}\boldsymbol{G}_1^{\mathrm{T}}\left(\boldsymbol{G}_1\boldsymbol{C}_{1,\mathrm{k}}\boldsymbol{G}_1^{\mathrm{T}}+\boldsymbol{I}\right)^{-1}\boldsymbol{G}_1\right]\boldsymbol{C}_{1,\mathrm{k}} \\
&\quad \left\{\mathrm{diag}\left[\left|\boldsymbol{S}_{1,\mathrm{k}}\right|^2\boldsymbol{R}_{1,\mathrm{k}}-\left(\boldsymbol{R}_{1,\mathrm{k}}\cdot\boldsymbol{S}_{1,\mathrm{k}}\right)\boldsymbol{S}_{1,\mathrm{k}}\right]\boldsymbol{m}_1^{\mathrm{k}-1}\right\}
\end{aligned}
\tag{11}
$$

After several simplifications of Eq. (11), the following equation can be obtained.

$$
\begin{aligned}
&\Delta\boldsymbol{m}_1+2\mu_1\frac{\mathrm{N}-1}{\mathrm{N}}\boldsymbol{C}_{1,\mathrm{k}}\left\{\mathrm{diag}\left[\left|\boldsymbol{S}_{1,\mathrm{k}}\right|^2\boldsymbol{R}_{1,\mathrm{k}}-\left(\boldsymbol{R}_{1,\mathrm{k}}\cdot\boldsymbol{S}_{1,\mathrm{k}}\right)\boldsymbol{S}_{1,\mathrm{k}}\right]\boldsymbol{m}_1^{\mathrm{k}-1}\right\} \\
&=\boldsymbol{C}_{1,\mathrm{k}}\boldsymbol{G}_1^{\mathrm{T}}\left(\boldsymbol{G}_1\boldsymbol{C}_{1,\mathrm{k}}\boldsymbol{G}_1^{\mathrm{T}}+\mathrm{I}\right)^{-1}\left\{\widehat{\boldsymbol{d}}_1^{\mathrm{k}}+2\mu_1\frac{\mathrm{N}-1}{\mathrm{N}}\boldsymbol{G}_1\boldsymbol{C}_{1,\mathrm{k}}\mathrm{diag}\left[\left|\boldsymbol{S}_{1,\mathrm{k}}\right|^2\boldsymbol{R}_{1,\mathrm{k}}-\left(\boldsymbol{R}_{1,\mathrm{k}}\cdot\boldsymbol{S}_{1,\mathrm{k}}\right)\boldsymbol{S}_{1,\mathrm{k}}\right]\boldsymbol{m}_1^{\mathrm{k}-1}\right\} \\
&=\boldsymbol{C}_{1,\mathrm{k}}\boldsymbol{G}_1^{\mathrm{T}}\boldsymbol{U}_{1,\mathrm{k}}^{-1}\boldsymbol{b}_1^{\mathrm{k}}
\end{aligned}
\quad , \tag{12}
$$

where $\boldsymbol{U}_{1,\mathrm{k}}=\boldsymbol{G}_1\boldsymbol{C}_{1,\mathrm{k}}\boldsymbol{G}_1^{\mathrm{T}}+\boldsymbol{I}$, $\boldsymbol{b}_1^{\mathrm{k}}=\widehat{\boldsymbol{d}}_1^{\mathrm{k}}+2\mu_1\frac{\mathrm{N}-1}{\mathrm{N}}\boldsymbol{G}_1\boldsymbol{C}_{1,\mathrm{k}}\mathrm{diag}\left[\left|\boldsymbol{S}_{1,\mathrm{k}}\right|^2\boldsymbol{R}_{1,\mathrm{k}}-\left(\boldsymbol{R}_{1,\mathrm{k}}\cdot\boldsymbol{S}_{1,\mathrm{k}}\right)\boldsymbol{S}_{1,\mathrm{k}}\right]\boldsymbol{m}_1^{\mathrm{k}-1}$, $\boldsymbol{U}_{1,\mathrm{k}}$ is a M × M-dimensional matrix and $\boldsymbol{b}_1^{\mathrm{k}}$ is a M-dimensional vector. From Eq. (10) and Eq. (12), it can be found that $\boldsymbol{G}_1^{T}\boldsymbol{G}_1+\boldsymbol{C}_{1,\mathrm{k}}^{-1}$ is a N × N-dimensional symmetric matrix, and $\boldsymbol{G}_1\boldsymbol{C}_{1,\mathrm{k}}\boldsymbol{G}_1^{\mathrm{T}}+\boldsymbol{I}$ is a M × M-dimensional symmetric matrix. In Eq. (12), $\boldsymbol{U}_{1,\mathrm{k}}^{-1}\boldsymbol{b}_1^{\mathrm{k}}$ can be solved by the inner loop of the ICG method and then convert the result from $\boldsymbol{U}_{1,\mathrm{k}}^{-1}\boldsymbol{b}_1^{\mathrm{k}}$ to the density model update with several matrices transformations. Obviously, $2\mu_1\frac{\mathrm{N}-1}{\mathrm{N}}\boldsymbol{C}_{1,\mathrm{k}}\left\{\mathrm{diag}\left[\left|\boldsymbol{S}_{1,\mathrm{k}}\right|^2\boldsymbol{R}_{1,\mathrm{k}}-\left(\boldsymbol{R}_{1,\mathrm{k}}\cdot\boldsymbol{S}_{1,\mathrm{k}}\right)\boldsymbol{S}_{1,\mathrm{k}}\right]\boldsymbol{m}_1^{\mathrm{k}-1}\right\}$ and $\boldsymbol{C}_{1,\mathrm{k}}\boldsymbol{G}_1^{\mathrm{T}}$ of Eq. (12) are simple matrices transformations, which will not consume too much computation cost. Therefore, it is necessary to change the calculation in the MS to the calculation in the DS, which makes fast computation speed and low memory cost. Additionally, the model update of the magnetization model has a similar form to that of the density model in Eq. (12).

The DS-ICG joint inversion method is used to recover physical property models of field data. In the inner loop of the ICG method, this section only needs to compute $\boldsymbol{U}_{1,\mathrm{k}}\boldsymbol{p}_1$, $\boldsymbol{p}_1$ is an arbitrary M-dimensional vector and the

remaining parts of the inner loop are the point calculations of the M-dimensional vectors, which demonstrates that the calculations of the inner loop in the DS are greatly reduced than that in the MS. Additionally, the DS-ICG method avoid computing $\boldsymbol{G}_1^{\mathrm{T}}\boldsymbol{G}_1$ in the GN method, and only need to calculate $\boldsymbol{G}_1\boldsymbol{t}_1$ and $\boldsymbol{G}_1^{\mathrm{T}}\boldsymbol{q}_1$. The computations of the above two matrices operations can be obtained by the forward problem. $\boldsymbol{t}_1$ and $\boldsymbol{q}_1$ are arbitrary N-dimensional and M-dimensional vectors, respectively. Therefore, the combination of the DS method and the ICG method for the correlation-analysis joint inversion can reduce the dimensions of calculation equation and then effectively reduce the computation cost.

The solution process of the DS-ICG joint inversion is similar to the solution process of the MS-ICG joint inversion in Algorithm 2 (Appendix B). Additionally, the calculation of $\boldsymbol{H}_{1,\mathrm{k}}^{-1}\boldsymbol{g}_1^{\mathrm{k}}$ is changed to compute $\boldsymbol{U}_{1,\mathrm{k}}^{-1}\boldsymbol{b}_1^{\mathrm{k}}$, and then $\boldsymbol{H}_{1,\mathrm{k}}$ and $\boldsymbol{g}_1^{\mathrm{k}}$ are replaced by $\boldsymbol{U}_{1,\mathrm{k}}$ and $\boldsymbol{b}_1^{\mathrm{k}}$ where $\boldsymbol{H}_{1,\mathrm{k}}$ and $\boldsymbol{g}_1^{\mathrm{k}}$ are called in Algorithm 2. Then, $\boldsymbol{m}_1^{\mathrm{k}} = \boldsymbol{m}_1^{\mathrm{k}-1} + \boldsymbol{x}_1^i$ in the MS-ICG joint method is changed to $\boldsymbol{m}_1^{\mathrm{k}} = \boldsymbol{m}_1^{\mathrm{k}-1} + \left\{\boldsymbol{C}_{1,\mathrm{k}}\boldsymbol{G}_1^{\mathrm{T}}\boldsymbol{x}_1^{\mathrm{i}} - 2\mu_1\frac{\mathrm{N}-1}{\mathrm{N}}\boldsymbol{C}_{1,\mathrm{k}}\mathrm{diag}\left[\left|\boldsymbol{S}_{1,\mathrm{k}}\right|^2\boldsymbol{R}_{1,\mathrm{k}} - \left(\boldsymbol{R}_{1,\mathrm{k}}\cdot\boldsymbol{S}_{1,\mathrm{k}}\right)\boldsymbol{S}_{1,\mathrm{k}}\right]\boldsymbol{m}_1^{\mathrm{k}-1}\right\}$ in the DS-ICG joint method. Additionally, the model update of the magnetization model in the DS-ICG joint inversion is consistent with the model update of the density model in the DS-ICG joint inversion.

3. Results and validation

Synthetic data and field data are used to verify the validity and applicability of the extended method in this paper. All computations are performed on an Intel(R)-Xeon(R)-CPU-E5-2600-V4 2.10-GHz machine with 123 Gbyte of RAM. The maximum memory cost during the joint inversion is shown in Table 1.

	Inversion method \ Meshing	$20\times20\times10$	$25\times25\times15$	$40\times40\times30$	$100\times100\times100$
Model 1	GN	0.520 GB	0.814 GB	9.119 GB	>123 GB
	MS-ICG	0.520 GB	0.797 GB	9.119 GB	>123 GB
	DS-ICG	0.461 GB	0.471 GB	0.537 GB	2.183 GB
	Inversion method \ Meshing	$20\times20\times10$	$40\times40\times20$	$50\times50\times50$	$100\times100\times100$
Model 2	MS-ICG	0.520 GB	4.323 GB	58.875 GB	>123 GB
	DS-ICG	0.461 GB	0.510 GB	0.670 GB	2.183 GB
	Inversion method \ Meshing	$24\times24\times10$	$40\times40\times40$	$50\times50\times50$	$100\times100\times100$
Field data	MS-ICG	0.591 GB	15.866 GB	58.960 GB	>123 GB
	DS-ICG	0.469 GB	0.610 GB	0.977 GB	2.869 GB

Table 1. Maximum memory cost during the calculations of different joint inversion methods.

3.1 Model 1

Figures 1a and 1b present a 3-D view of the model 1. The data on the surface are generated on a grid with $21\times21=441$ points and grid spacing 100 m. The gravity and magnetic data computed from model 1 are illustrated in Figures 1c and 1d, respectively. To perform the inversion, the subsurface volume is discretized into $20\times20\times10$

prisms of sizes 100 m in each dimension. For all inversions, the bound constraints $0 = \mathrm{m}_1^- \leq \boldsymbol{m}_1 \leq \mathrm{m}_1^+ = 1.0$, g/cc, and $0 = \mathrm{m}_2^- \leq \boldsymbol{m}_2 \leq \mathrm{m}_2^+ = 1.0$, A/m, are imposed.

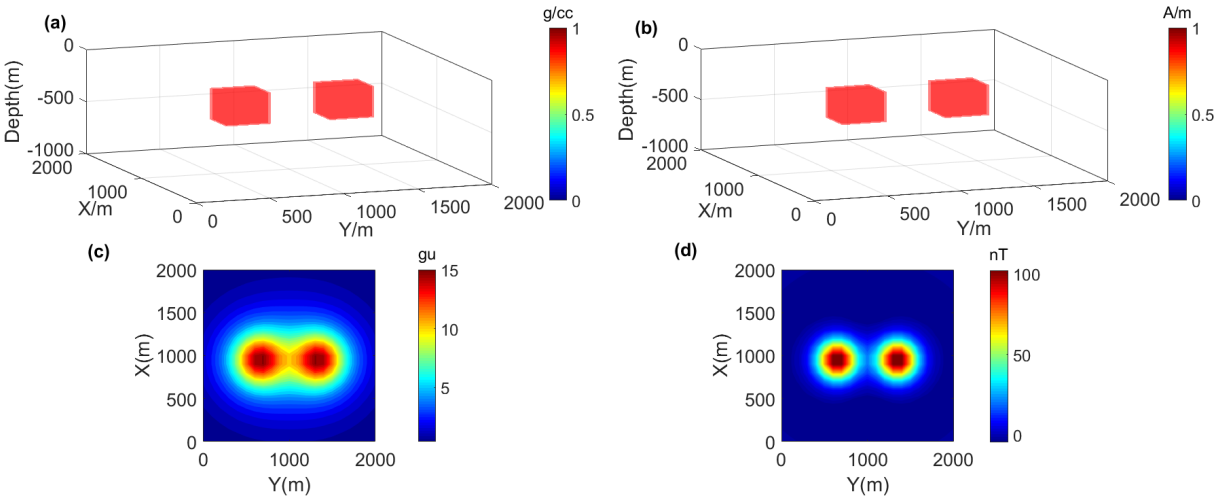

Figure 1. (a) Spatial location of the synthetic model 1 for density model. (b) Spatial location of the synthetic model 1 for magnetization model. (c) The contour map of forward gravity anomaly of synthetic model 1. (d) The contour map of forward magnetic anomaly of synthetic model 1.

Firstly, the separate inversions of gravity and magnetic data are performed based on the GN method and the stabilization function of the minimum difference between the recovered model and the reference model, respectively. The L-curve method is used to acquire the suitable regularization parameters.

Fig. 2a presents the L curve of gravity data, and the obtained regularization parameter is 2.8×10^8. Set the initial density model to 0.01 g/cc and the reference density model to 0.0 g/cc. Then, the separate inversion of gravity data is performed. Figures 2b and 2c present the slices of the reconstructed density model at x = 1000 m and z = 400 m, respectively. Figure 2d is the L curve of the magnetic data, and the obtained regularization parameter is 6.3×10^{10}.

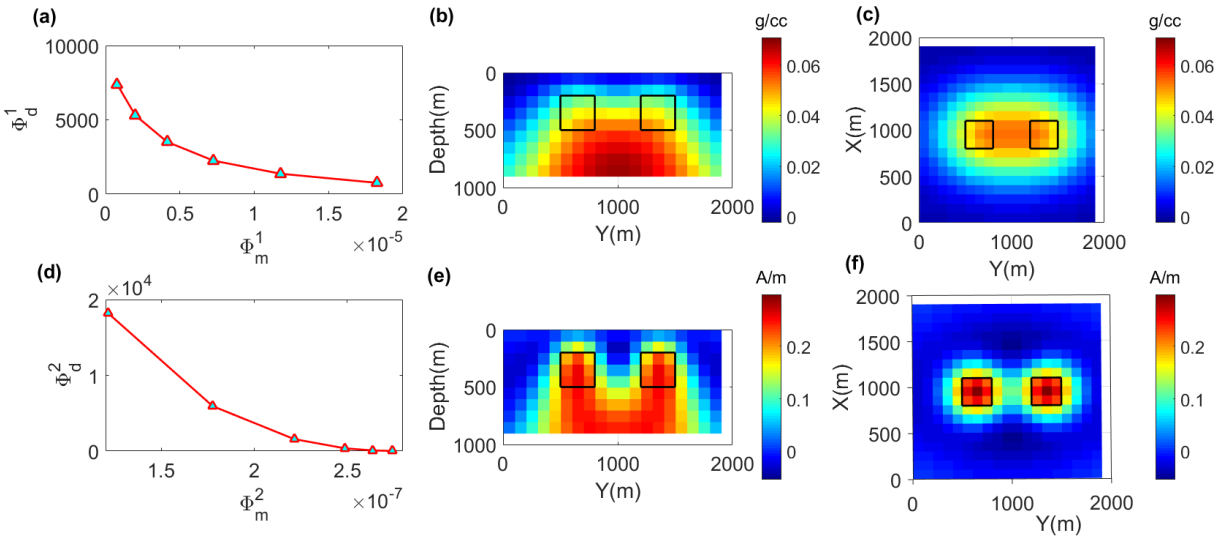

Figure 2. (a) The L curve method is used to calculate the regularization parameter of the gravity data; (d) The L curve method is used to calculate the regularization parameter of the magnetic data; (b) and (c) are the slices of recovered density model at x = 1000 m and z = 400 m, respectively. (c) and (f) are the slices of recovered magnetization model at x = 1000 m and z = 400 m, respectively. The black boxes are the locations of the real models.

Set the initial magnetization model to 0.01 A/m and the reference magnetization model to 0.0 A/m. Then, the separate inversion of magnetic data is performed. Figures 2e and 2f show the slices of reconstructed magnetization model at x = 1000 m and z = 400 m, respectively. The recovered density model and recovered magnetization model obtained by the separate inversions are adopted to the initial density model and initial magnetization model for the joint inversion by the GN method, respectively. Additionally, the obtained regularization parameters are also brought into the joint inversion.

Secondly, the joint inversion is performed by the GN method, and the CG method is used to calculate the model update vector. The weighting parameters of the correlation-analysis constraints of the gravity and magnetic data are set to 1.0×10^5 and 1.0×10^4, respectively.

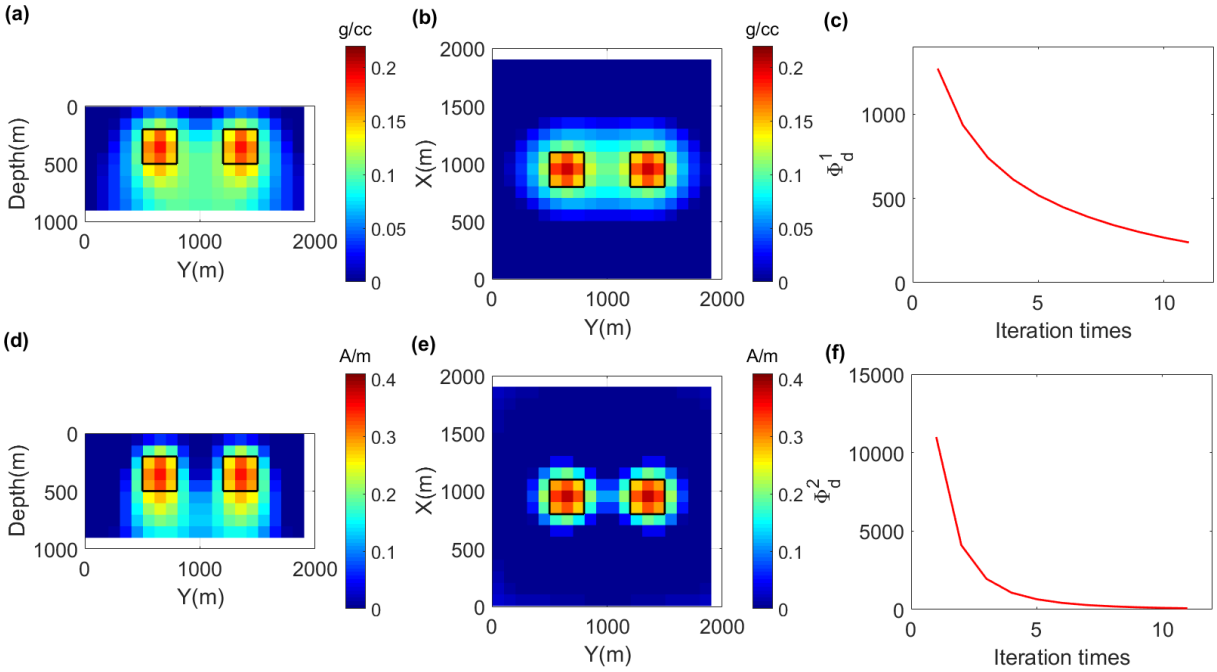

Figure 3. The joint inversion of synthetic data 1 based on the GN method. (a) and (b) are the slices of recovered density model at x = 1000 m and z = 400 m, respectively. (d) and (e) are the slices of recovered magnetization model at x = 1000 m and z = 400 m, respectively. Convergence curves of the correlation-analysis joint inversion of gravity data (c) and magnetic data (f). The black boxes are the locations of the real models.

Figures 3a and 3b present the slices of the recovered density model at x = 1000 m and z = 400 m, respectively. Figures 3d and 3e present the slices of the recovered magnetization model at x = 1000 m and z = 400 m, respectively. Figures 3c and 3f are convergence curves of the joint inversion of gravity and magnetic data, respectively, and the calculation time is 18 minutes. From Figure 3, the recovered models roughly describe the distribution of the real sources.

Then, the joint inversion based on the same stable function in the previous joint inversion is performed by the MS-ICG method. The weighting parameters of the correlation-analysis constraints are set to 1.0×10^4 and 1.0×10^3, respectively. The number of iterations of the outer loop and the inner loop are set to 10 and 15, respectively. The initial density model and the initial magnetization model are set to 0.01 g/cc and 0.01 A/m, respectively. Then, the MS-ICG joint inversion is performed.

Figures 4a and 4b present the slices of reconstructed density model at x = 1000 m and at z = 400 m, respectively. Figures 4d and 4e show the slices of recovered magnetization model at x = 1000 m at z = 400 m, respectively. Figures 4c and 4f are convergence curves of the joint inversion of gravity and magnetic data, respectively, and the computation time is 12 minutes. Comparing the recovered results in Figures 3 and 4, it can be found that there is no significant difference between the two recovered results, and the computation time of the latter inversion is relatively short.

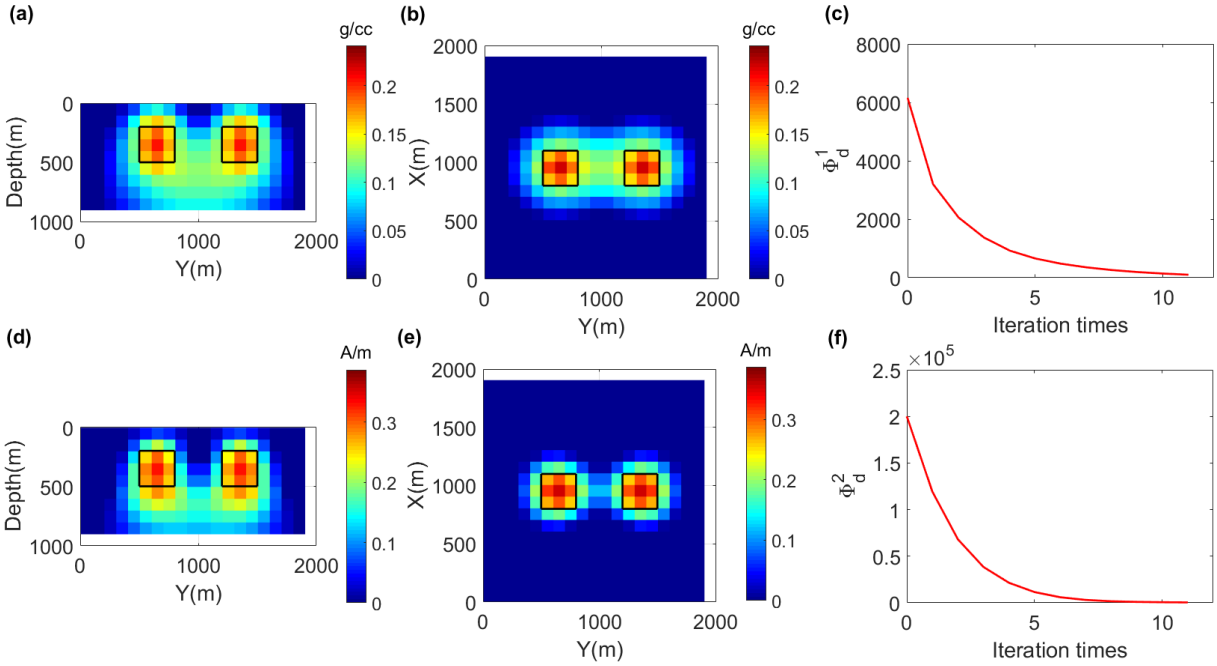

Figure 4. The joint inversion of synthetic data 1 based on the MS-ICG method and the L2-norm regularization method. (a) and (b) are the slices of recovered density model at x = 1000 m and z = 400 m, respectively. (d) and (e) are the slices of recovered magnetization model at x = 1000 m and z = 400 m, respectively. Convergence curves of the correlation-analysis joint inversion of gravity data (c) and magnetic data (f) in the MS. The black boxes are the locations of the real models.

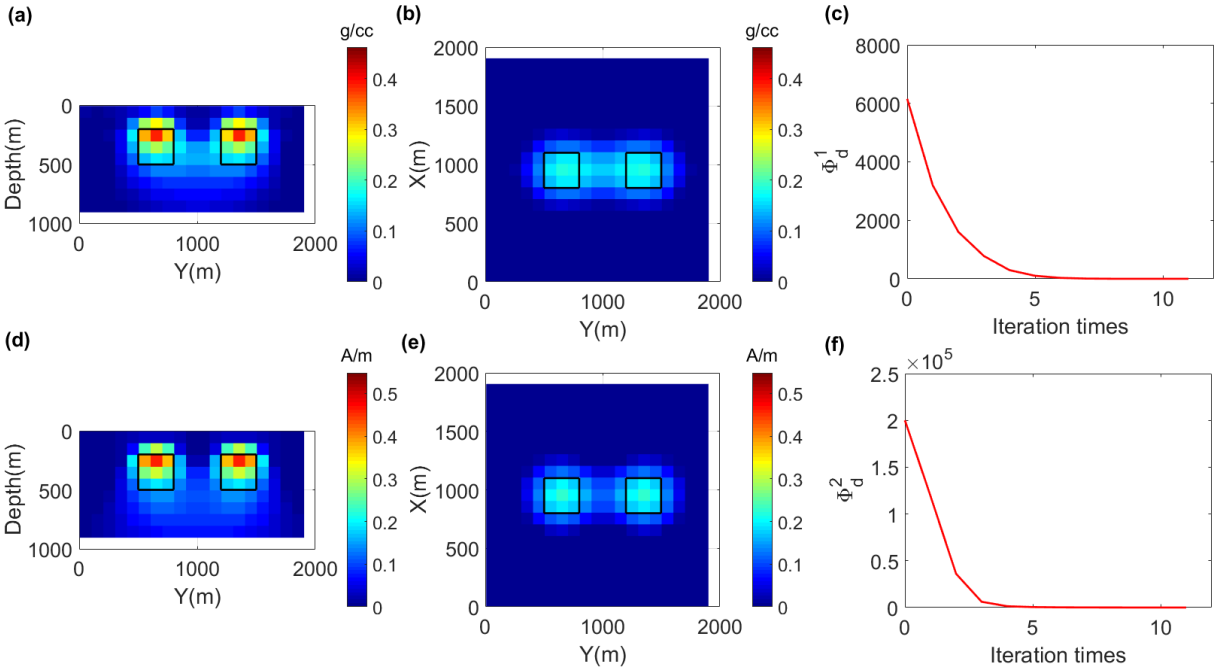

Figure 5. The MS-ICG joint inversion of synthetic data 1. (a) and (b) are the slices of recovered density model at x = 1000 m and z = 400 m, respectively. (d) and (e) are the slices of t recovered magnetization model at x = 1000 m and z = 400 m, respectively. Convergence curves of the MS-ICG joint inversion of gravity data (c) and magnetic data (f). The black boxes are the locations of the real models.

Then, the MS-ICG joint inversion based on the elastic-nets regularized method is performed. The parameters are set to $\tau_1 = 0.6$, $\tau_2 = 0.6$ and $\varepsilon = 0.001$, and the other parameters are consistent with those parameters in the previous joint inversion performed by the GN method.

Figures 5a and 5b show the slices of the recovered density model at x = 1000 m and at z = 400 m, respectively. Figures 5d and 5e present the slices of the recovered magnetization model at x = 1000 m and at z = 400 m, respectively. Figures 5c and 5f are convergence curves of the joint inversion of gravity and magnetic data, respectively, and the calculation time is 11 minutes and 3 seconds. From Figures 3, 4 and 5, it can be found that when the stable function with sparse factor and the ICG method are adopted, the reconstructed models are closer to the real models and show clear boundaries.

Then, the DS-ICG separate inversions of gravity and magnetic data based on the elastic-nets regularized method is performed. The parameters used are consistent with those parameters of the MS-ICG joint inversion.

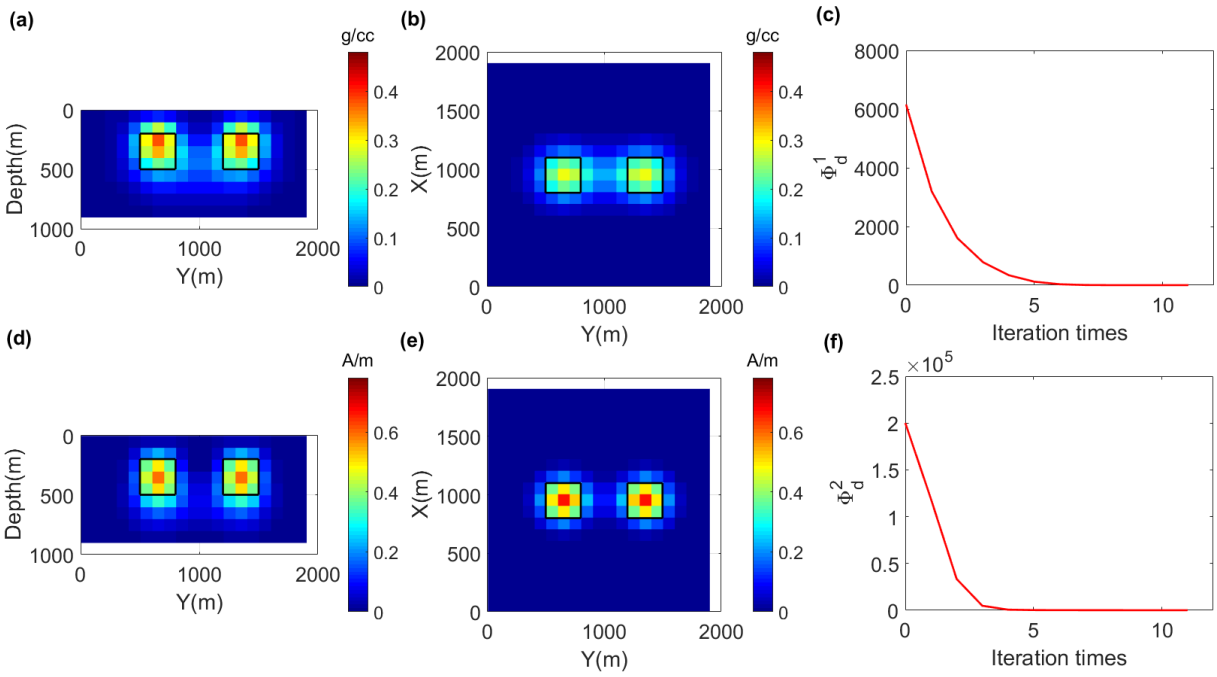

Figure 6. The separate inversions of synthetic data 1 based on the DS-ICG method. (a) and (b) are the slices of recovered density model at x = 1000 m and z = 400 m, respectively. (d) and (e) are the slices of recovered magnetization model at x = 1000 m and z = 400 m, respectively. Convergence curves of the separate inversions of gravity data (c) and magnetic data (f) in the DS. The black boxes are the locations of the real models.

Figures 6a and 6b present the slices of the recovered density model at x = 1000 m and at z = 400 m, respectively. Figures 6d and 6e present the slices of the recovered magnetization model at x = 1000 m and at z = 400 m, respectively. Figures 6c and 6f are convergence curves of the separate inversions of gravity and magnetic data, respectively. Obviously, the DS-ICG method adopted to the separate inversions, and the recovered results are significantly improved.

Next, the DS-ICG joint inversion based on the elastic-nets regularized method is performed. The weighting parameters of the correlation-analysis constraints are set to 5.0 and 1.0, respectively, and the other parameters are consistent with those parameters of the MS-ICG joint inversion

Figures 7a and 7b present the slices of the reconstructed density models, respectively. Figures 7d and 7e present the slices of the recovered magnetization model, respectively. Figures 7c and 7f are convergence curves of the DS-ICG joint inversion of gravity and magnetic data, respectively, and the joint inversion time is 3 minutes and 15 seconds. Comparing the recovered results shown in Figures 3, 4, 5, 6 and 7, it can be found that the reconstructed models obtained by the DS-ICG joint inversion method present the best performance that the numerical value and the spatial distribution of the recovered models are closer to the real models, suggesting the correctness and advantages of the extended method in this paper.

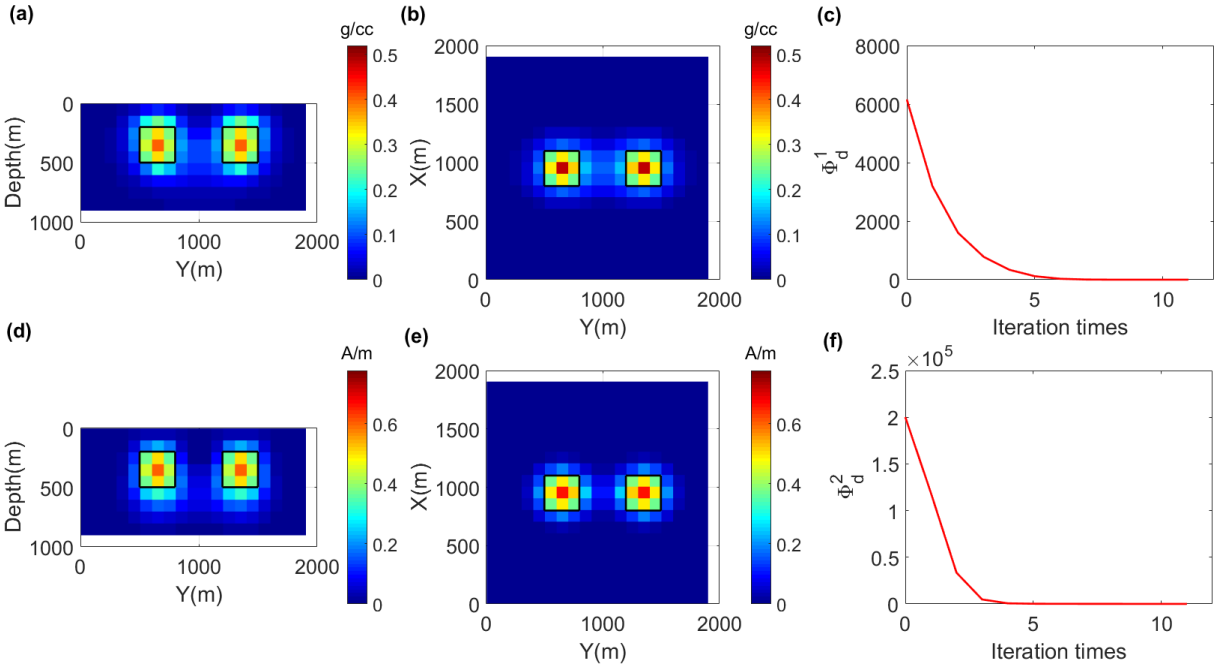

Figure 7. The DS-ICG joint inversion of synthetic data 1. (a) and (b) are the slices of recovered density model at x = 1000 m and z = 400 m, respectively. (d) and (e) are the slices of recovered magnetization model at x = 1000 m and z = 400 m, respectively. Convergence curves of the DS-ICG joint inversion of gravity data (c) and magnetic data (f). The black boxes are the locations of the real models.

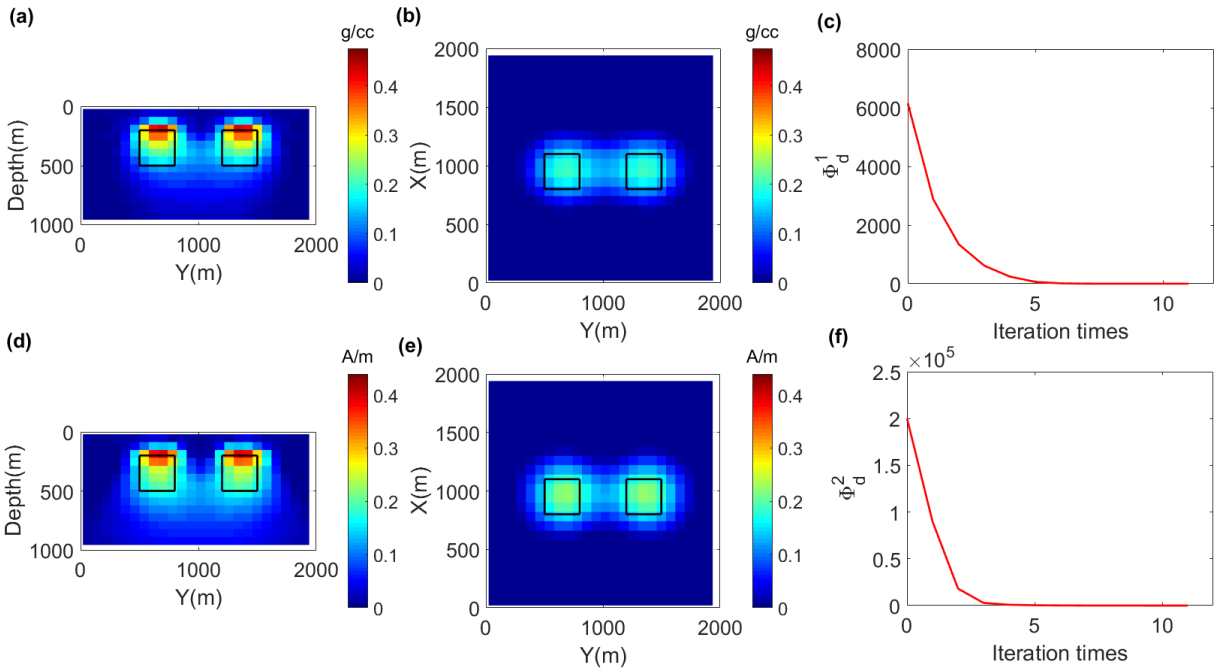

Figure 8. The MS-ICG joint inversion of synthetic data 1. (a) and (b) are the slices of t recovered density model at x = 1000 m and z = 400 m, respectively. (d) and (e) are the slices of recovered magnetization model at x = 1000 m and z = 400 m, respectively. Convergence curves of the MS-ICG joint inversion of gravity data (c) and magnetic data (f). The black boxes are the locations of the real models.

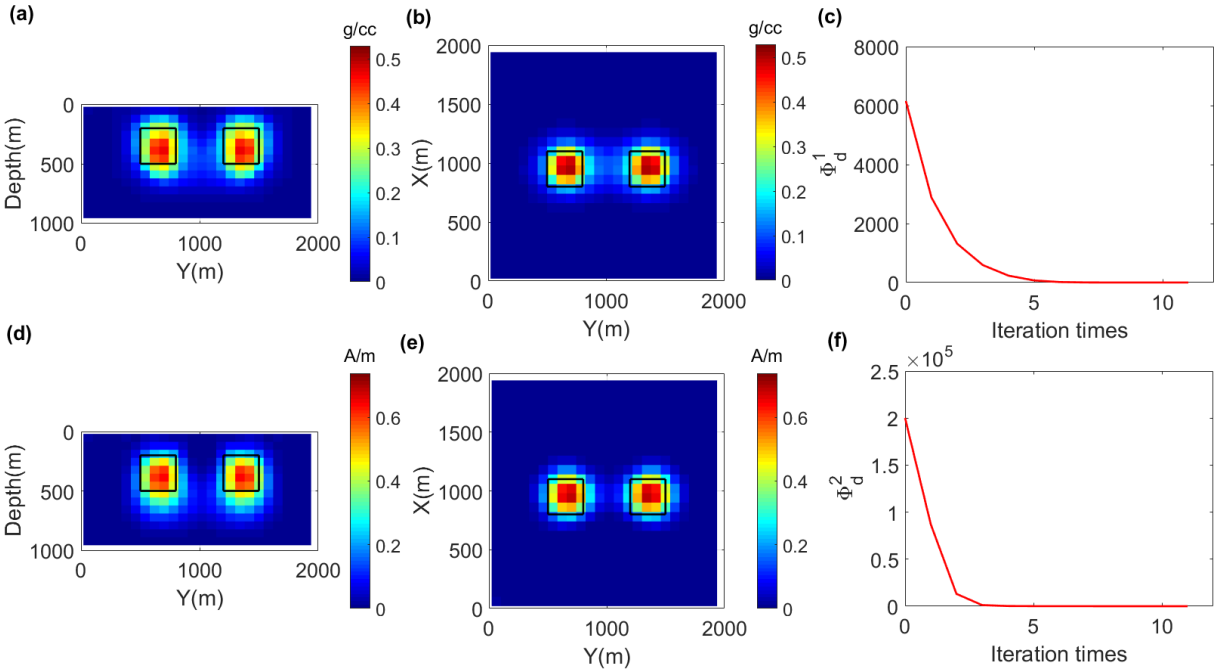

Figure 9. The DS-ICG joint inversion of synthetic data 1. (a) and (b) are the slices of t recovered density model at x = 1000 m and z = 400 m, respectively. (d) and (e) are the slices of recovered magnetization model at x = 1000 m and z = 400 m, respectively. Convergence curves of the DS-ICG joint inversion of gravity data (c) and magnetic data (f). The black boxes are the locations of the real models.

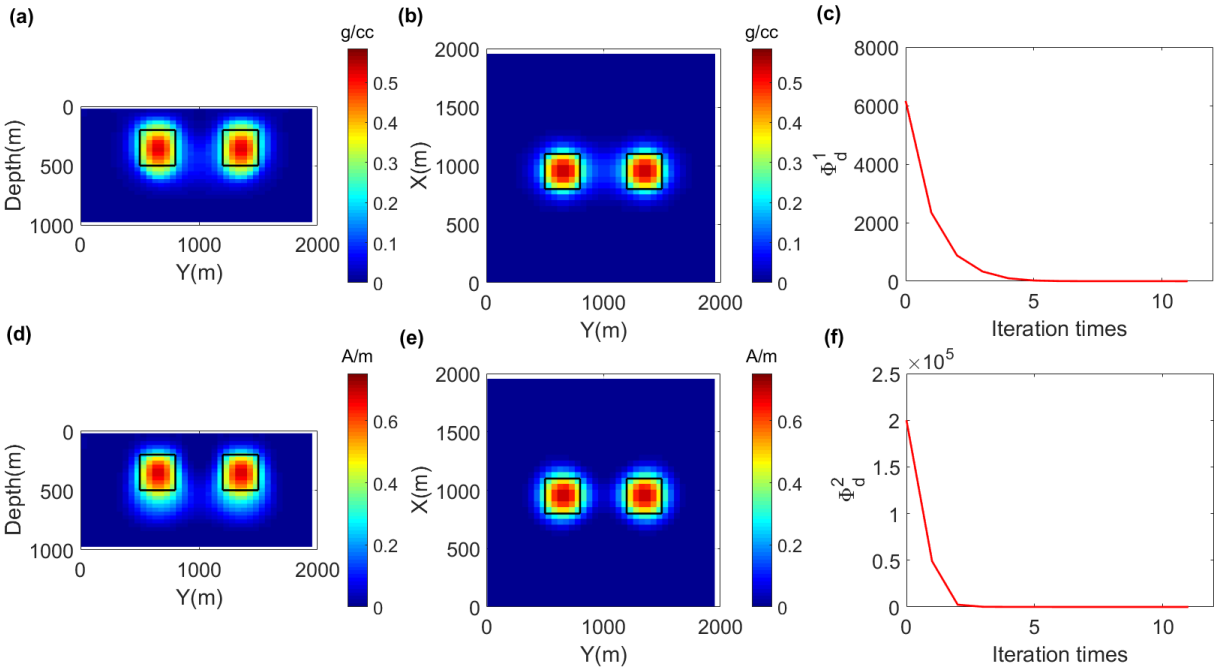

Figure 10. The DS-ICG joint inversion of synthetic data 1. (a) and (b) are the slices of recovered density model at x = 1000 m and z = 400 m, respectively. (d) and (e) are the slices of recovered magnetization model at x = 1000 m and z = 400 m, respectively. Convergence curves of the DS-ICG joint inversion of gravity data (c) and magnetic data (f). The black boxes are the locations of the real models.

Furthermore, the subsurface volume is discretized into $25 \times 25 \times 15$ prisms to verify the efficiency of the extended method in this paper. Firstly, the MS-ICG joint inversion based on the elastic-nets regularized method is performed, and the weighting parameters of the correlation-analysis constraints are set to 1.0×10^3 and 1.0×10^2, respectively. The remaining parameters are consistent with those parameters of the previous MS-ICG joint inversion.

Figures 8a, 8b, 8d and 8e present the slices of the reconstructed models, respectively. Figures 8c and 8f are convergence curves of the DS-ICG joint inversion of gravity and magnetic data, respectively, and the joint inversion time is 55 minutes. Then, the weighting parameters of the correlation-analysis constraints are changed to 0.5 and 0.1, respectively, the remaining parameters are consistent with those parameters of the MS-ICG joint inversion and then the DS-ICG joint inversion based on the elastic-nets regularized method is performed.

Figures 9a, 9b, 9d and 9e present the slices of the reconstructed models, respectively. Figures 9c and 9f are convergence curves of the DS-ICG joint inversion of gravity and magnetic data, respectively, and the inversion time is 8 minutes. Additionally, the meshing is refined to $40 \times 40 \times 30$ prisms to verify the efficiency of the extended method. The parameters of the correlation-analysis constraints are changed to 0.01 and 0.01, respectively. The remaining parameters are consistent with those parameters of the previous DS-ICG joint inversion.

Figures 10a, 10b, 10d and 10e present the slices of the reconstructed models, respectively, and the calculation time is 50 minutes. Comparing the computation time of the joint inversions mentioned above, it can be shown that the calculation efficiency of the DS-ICG joint inversion is higher than the calculation efficiency of the MS-ICG joint inversion. From the recovered models shown in Figures 8, 9 and 10, it can be seen that the DS-ICG joint inversion improves the inversion accuracy, which illustrates the correctness and advantages of the extended method in this paper. Additionally, the part of model 1 in Table 1 shows that the DS-ICG joint inversion method requires less memory cost, which again proves the high efficiency of the extended method in this paper.

3.2 Model 2

A more complicated model is used to verify the applicability of the extended method in this paper. Figures 11a and 11b present a 3-D view of the synthetic model 2. The data on the surface are generated on a grid with $21 \times 21 = 441$ points and grid spacing 100 m. The gravity and magnetic data computed from model 2 are presented in Figs. 11c and 11d, respectively. To perform the inversion, the subsurface volume is discretized into $20 \times 20 \times 10$ prisms of sizes 100 m in each dimension. For all inversions, the bound constraints $0 = \mathrm{m}_1^- \leq \boldsymbol{m}_1 \leq \mathrm{m}_1^+ = 1.0$, g/cc, and $0 = \mathrm{m}_2^- \leq \boldsymbol{m}_2 \leq \mathrm{m}_2^+ = 1.0$, A/m, are imposed.

Firstly, the numbers of iterations of the outer loop and the inner loop are both set to 10. The initial density model and the initial magnetization model are set to 0.01 g/cc and 0.01 A/m, respectively. Obviously, the regularization method is closer to the L1 norm, the more obvious boundaries of the recovered models will be obtained. Therefore, the regularization method is made close to the L1-norm regularization method in the inversions of synthetic data 2 and the related parameters are set to $\tau_1 = 0.01$, $\tau_2 = 0.01$, $\varepsilon = 0.001$, and those parameters are used for the subsequent inversions of synthetic data 2. Then, the separate inversions of gravity and magnetic data are performed by the MS-ICG method, respectively.

Figures 12a and 12b present the slices of the reconstructed density model, respectively. Figures 12d and 12e present the slices of the reconstructed magnetization model, respectively. Figures 12c and 12f are convergence curves of the MS-ICG separate inversions of gravity and magnetic data, respectively.

The weighting parameters and the numbers of iterations are very important for the inversion. The iteration numbers of the outer loop and the inner loop are set to 10 and 25, the weighting parameters of the correlation-analysis constraints for gravity data and magnetic data are both set to 7.0. The other parameters are consistent with those parameters of the previous MS-ICG separate inversions of synthetic data 2 and then the MS-ICG joint inversion is performed.

Figures 13a and 13b show the slices of the reconstructed density models, respectively. Figures 13d and 13e show the slices of the recovered magnetization model, respectively. Figs. 13c and 13f are convergence curves of the MS-ICG joint inversion of gravity and magnetic data, respectively, and the joint inversion time is 13 minutes and 23 seconds. From Figures 12 and 13, the recovered physical models from the MS-ICG joint inversion show better performance that the distribution and the values of the recovered models are closer to the real models.

Next, the DS-ICG inversion method is adopted to carry out separate inversions of the gravity and magnetic data, respectively. The iteration numbers of the outer loop and the inner loop are both set to 10 and the other parameters

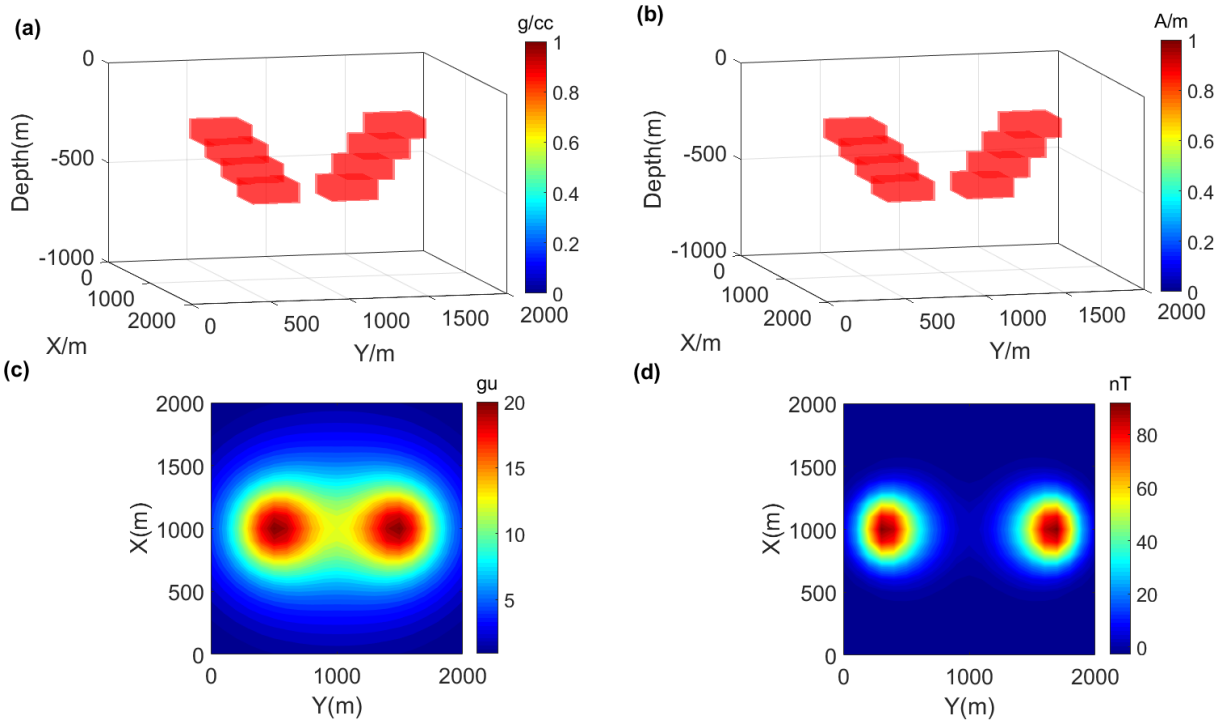

Figure 11. (a) Spatial location of the synthetic model 2 for density model. (b) Spatial location of the synthetic model 2 for magnetization model. (c) The contour map of forward gravity anomaly of model 2. (d) The contour map of forward magnetic anomaly of model 2.

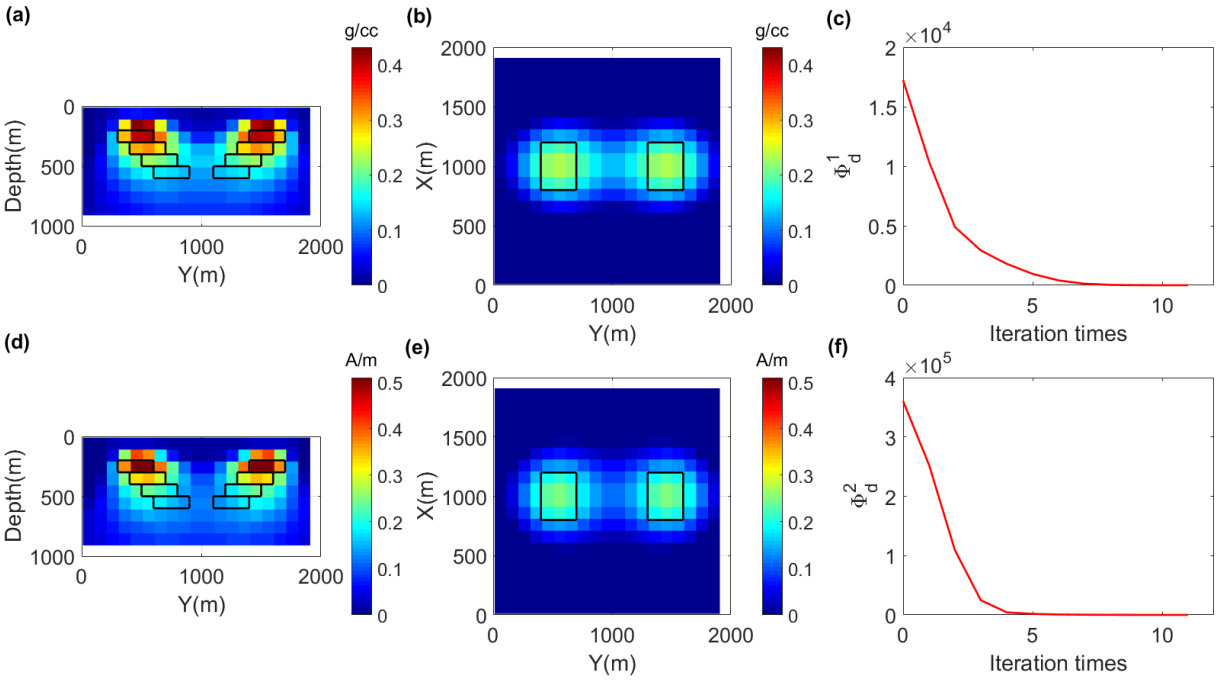

Figure 12. The MS-ICG separate inversions of synthetic data 2. (a) and (b) are the slices of recovered density model at x = 1000 m and z = 400 m, respectively. (d) and (e) are the slices of recovered magnetization model at x = 1000 m and z = 400 m, respectively. Convergence curves of the separate inversions of gravity data (c) and magnetic data (f) in the MS. The black boxes are the locations of the real models.

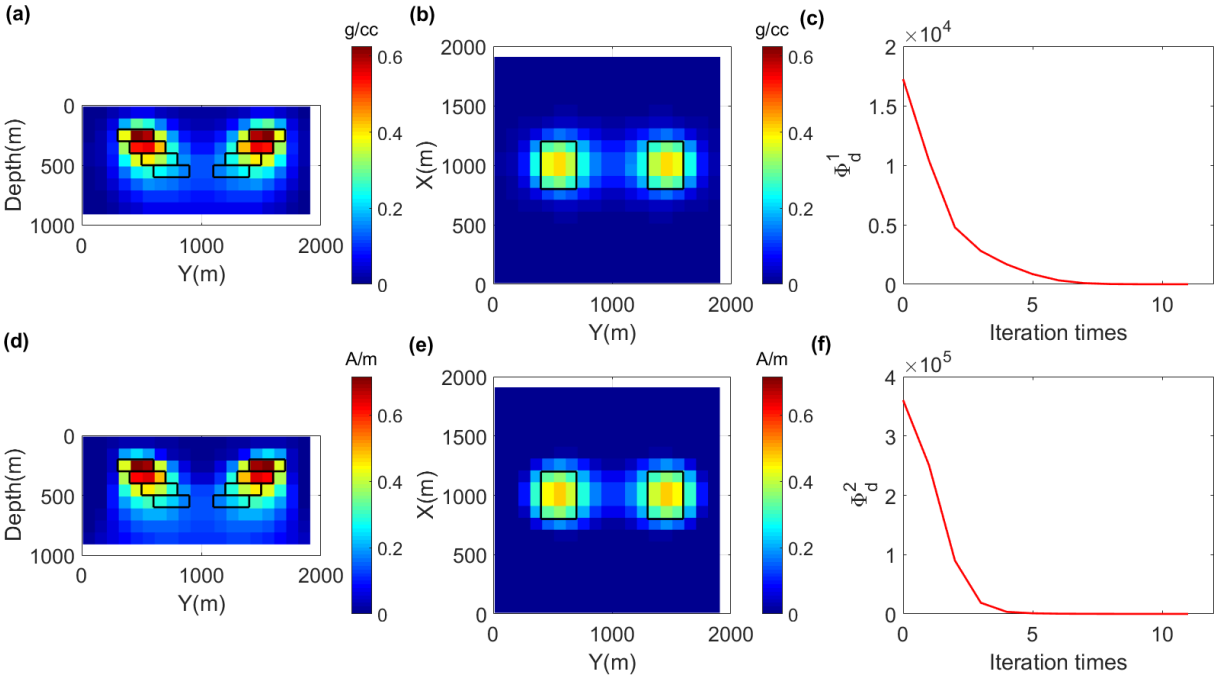

Figure 13. The MS-ICG joint inversion of synthetic data 2. (a) and (b) are the slices of recovered density model at x = 1000 m and z = 400 m, respectively. (d) and (e) are the slices of recovered magnetization model at x = 1000 m and z = 400 m, respectively. Convergence curves of the MS-ICG joint inversion of gravity data (c) and magnetic data (f). The black boxes are the locations of the real models.

are consistent with those parameters of the previous MS-ICG separate inversions on synthetic data 2 and then the DS-ICG separate inversions are performed.

Figures 14a and 14b present the slices of the recovered density model, respectively. Figures 14d and 14e show the slices of the reconstructed magnetization model, respectively. Figures 14c and 14f are convergence curves of the DS-ICG separate inversions of gravity and magnetic data, respectively.

Then, the weighting parameters of the correlation-analysis constraints are both set to 1.0. The iteration numbers of the outer loop and the inner loop of the joint inversion are both set to 10, the other parameter values are consistent with those parameters in the MS-ICG joint inversion, and then the DS-ICG joint inversion is performed.

Figures 15a and 15b show the slices of the recovered density model, respectively. Figures 15d and 15e show the slices of the reconstructed magnetization model, respectively. Figures 15c and 15f are convergence curves of the DS-ICG joint inversion of gravity and magnetic data, respectively, and the joint inversion time is 3 minutes and 13 seconds. From Figures 12, 13, 14 and 15, the recovered models obtained by the DS-ICG joint method are more reasonable, which is shown that the 3D spatial distribution and the values of the recovered models are closer to the real models. Furthermore, the subsurface volume is discretized into $40 \times 40 \times 20$ prisms to verify the efficiency of the extended method in this paper. The parameters of the correlation-analysis constraints are changed to 0.2 and 0.2, respectively. The remaining parameter values are the same as those parameters of the previous DS-ICG joint inversion and then the DS-ICG joint inversion is performed.

Figures 16a, 16b, 16d and 16e show the slices of the reconstructed models, respectively. Figures 16c and 16f are convergence curves of the DS-ICG joint inversion of gravity and magnetic data, respectively, and the joint inversion time is 38 minutes. It can be found that the DS-ICG joint inversion can acquire the reasonable recovered results in a short period of time, suggesting the correctness of the method extended in this paper. Additionally, the part of Model 2 in Table 1 can be found that the DS-ICG joint inversion method requires less memory resources than the MS-ICG joint inversion method, which can illustrate the high efficiency of the extended method in this paper.

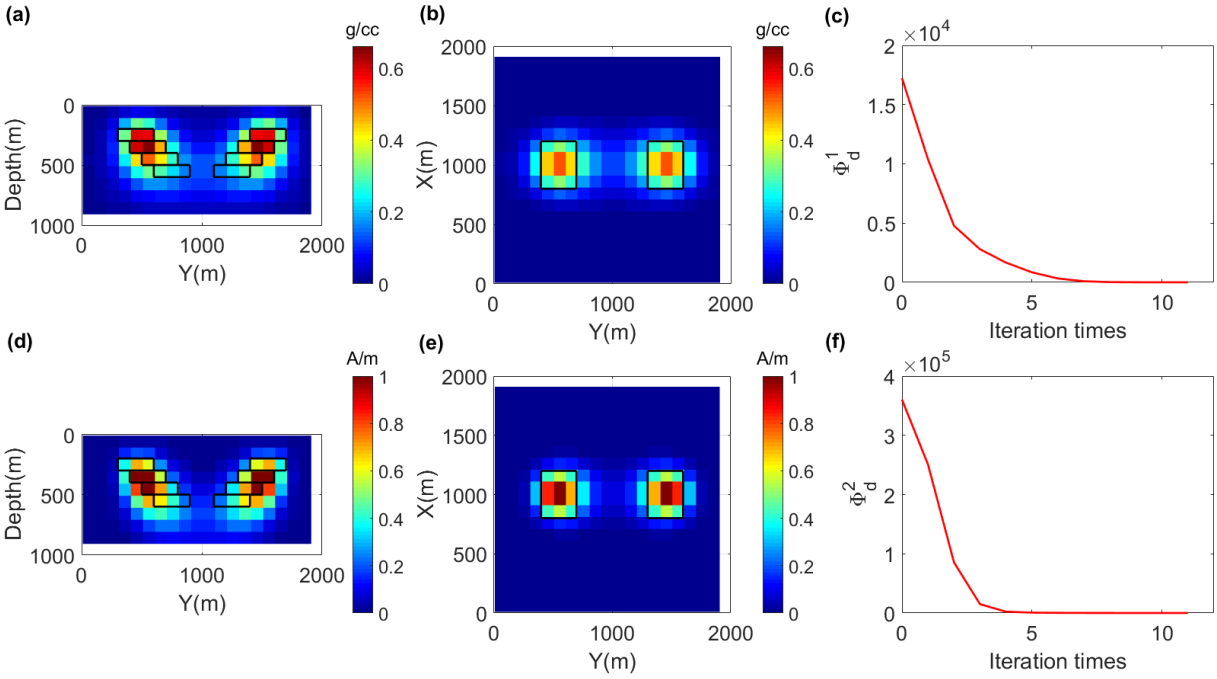

Figure 14. The DS-ICG separate inversions of synthetic data 2. (a) and (b) are recovered density model at x = 1000 m and z = 400 m, respectively. (d) and (e) are the slices of recovered magnetization model at x = 1000 m and z = 400 m, respectively. Convergence curves of the separate inversions of gravity data (c) and magnetic data (f) in the DS. The black boxes are the locations of the real models.

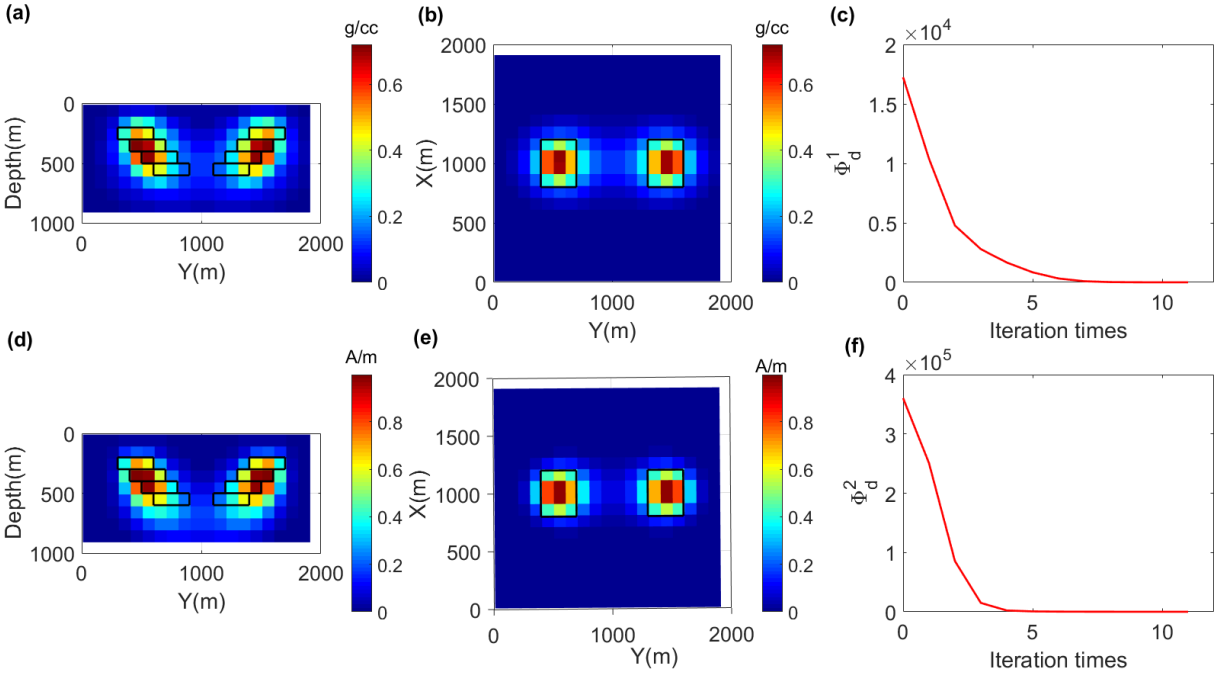

Figure 15. The DS-ICG joint inversion of synthetic data 2. (a) and (b) are the slices of recovered density model at x = 1000 m and z = 400 m, respectively. (d) and (e) are the slices of recovered magnetization model at x = 1000 m and z = 400 m, respectively. Convergence curves of the DS-ICG joint inversion for gravity data (c) and magnetic data (f). The black boxes in the figure 15 are the locations of the real models.

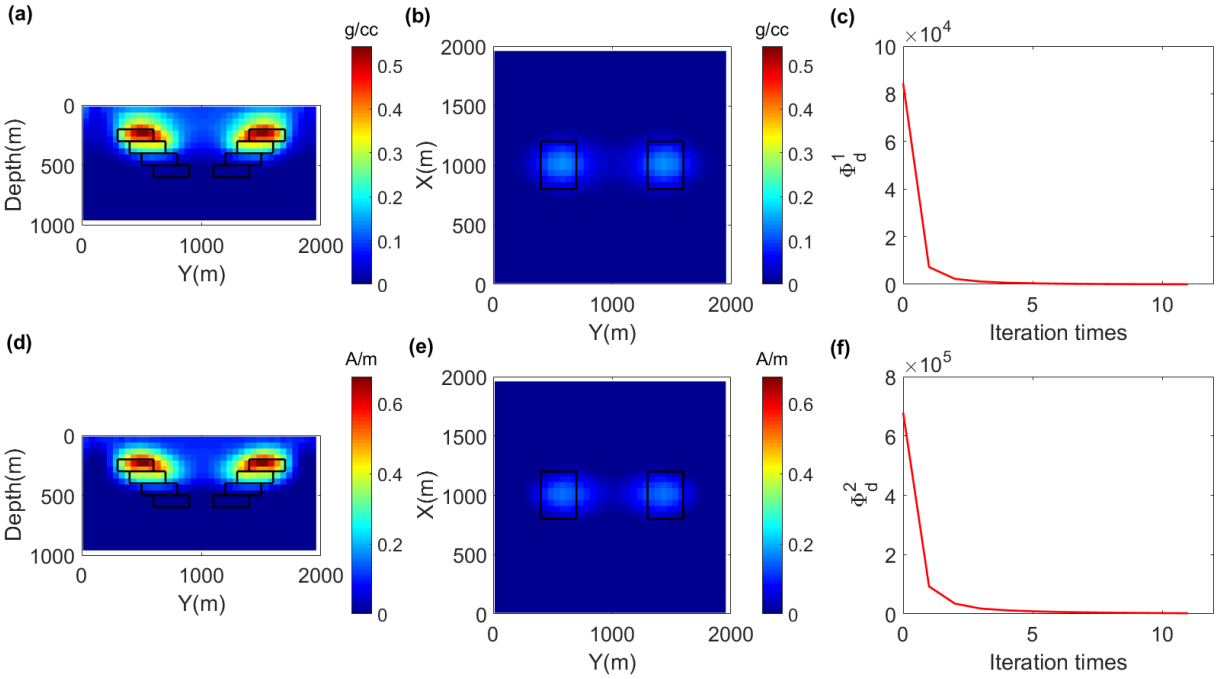

Figure 16. The DS-ICG joint inversion of synthetic data 2. (a) and (b) are the slices of recovered density model at x = 1000 m and z = 400 m, respectively. (d) and (e) are the slices of recovered magnetization model at x = 1000 m and z = 400 m, respectively. Convergence curves of the DS-ICG joint inversion of gravity data (c) and magnetic data (f). The black boxes in the figure 16 are the locations of the real models.

3.3 Validation by the Field Data

The correlation-analysis joint inversion is applied to the interpretation of field data in the Pingbao lead-zinc-silver polymetallic mining area in Hunan Province, China. After removing the regional gravity anomalies from the observed gravity anomalies, the residual gravity anomalies (Figure 17a) are obtained. Simultaneously, regional magnetic field is subtracted from the observed magnetic anomaly data (Figure 17b).

The observation network of gravity and magnetic data is a regular grid of 25 × 25, with a total of 625 equidistant data points. The subsurface volume is discretized into 24 × 24 × 10 prisms. We assume that the value of each of the inverted parameters is uniform within each cell. From prior petrophysical information obtained from the borehole data in the mining area, the bound constraints $-0.3 = m_1^- \leq \boldsymbol{m}_1 \leq m_1^+ = 5.0$, g/cc, and $0.6 = m_2^- \leq \boldsymbol{m}_2 \leq m_2^+ = 4.0$, A/m, are imposed.

Firstly, the MS-ICG joint inversion based on the elastic-nets regularized method is performed on gravity and magnetic data, and the initial density model and the initial magnetization model are uniform half-space model with 0.1 g/cc and 0.1 A/m, respectively. The parameters values are set to $\tau_1 = 0.4$, $\tau_2 = 0.4$ and $\varepsilon = 0.01$. Additionally, the iteration numbers of the outer loop and the inner loop are set to 20 and 15, respectively. The weighting parameters of the correlation-analysis constraints are set to 0.2 and 0.1, respectively. Then, the MS-ICG joint inversion of field data is performed.

Figures 18a, 18b and 18c present the slices of the reconstructed density model at z = 250 m, z = 450 m and z = 650 m, respectively. Figures 18e, 18f and 18g present the slices of the recovered magnetization model at z = 250 m, z = 450 m and z = 650 m, respectively. Figures 18d and 18h are convergence curves of the joint inversion of gravity and magnetic data, respectively, and the joint inversion time is 60 minutes and 30 seconds. Furthermore, the DS-ICG joint inversion based on the elastic-nets regularized method is performed on gravity and magnetic data. The iteration numbers of the outer loop and the inner loop are set to 17 and 15, respectively. The weighting parameters of the correlation-analysis constraints for gravity and magnetic data are set to 5.0×10^{-4} and 1.0×10^{-5}, respectively. The remaining parameter values are the same as those parameters of the previous MS-ICG joint inversion.

Figures 19a, 19b and 19c show the slices of the reconstructed density model at z = 250 m, z = 450 m and z = 650 m, respectively. Figures 19e, 19f and 19g show the slices of the reconstructed magnetization model at z = 250 m, z = 450 m

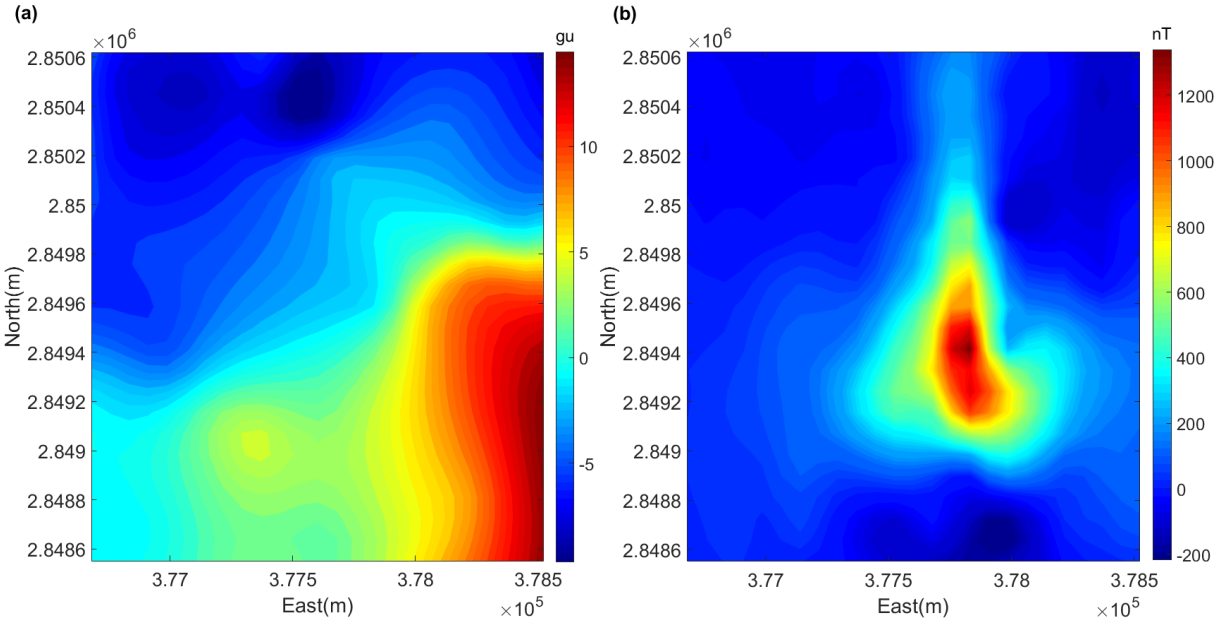

Figure 17. (a) Residual gravity anomaly data in Huangshaping mining area, Hunan Province. (b) Residual magnetic anomaly data in Huangshaping mining area, Hunan Province.

and z = 650 m, respectively. Figures 19d and 19h are convergence curves of the joint inversion of gravity and magnetic data, respectively, and the joint inversion time is 14 minutes and 14 seconds. Obviously, the calculation time in the DS is much shorter than the calculation time in the MS.

From Figs. 18 and 19, it can be found that the recovered models can distinguish the distributions of the subsurface bodies. The distribution of the reconstructed density model is well corresponding to the distribution of the gravity anomaly, showing a trend of high values in the southeastern region and low values in the northeastern region. Simultaneously, the distribution of the recovered magnetization model also has a good correspondence to the distribution of the magnetic anomaly, showing a trend of high values in the middle area and low values on both

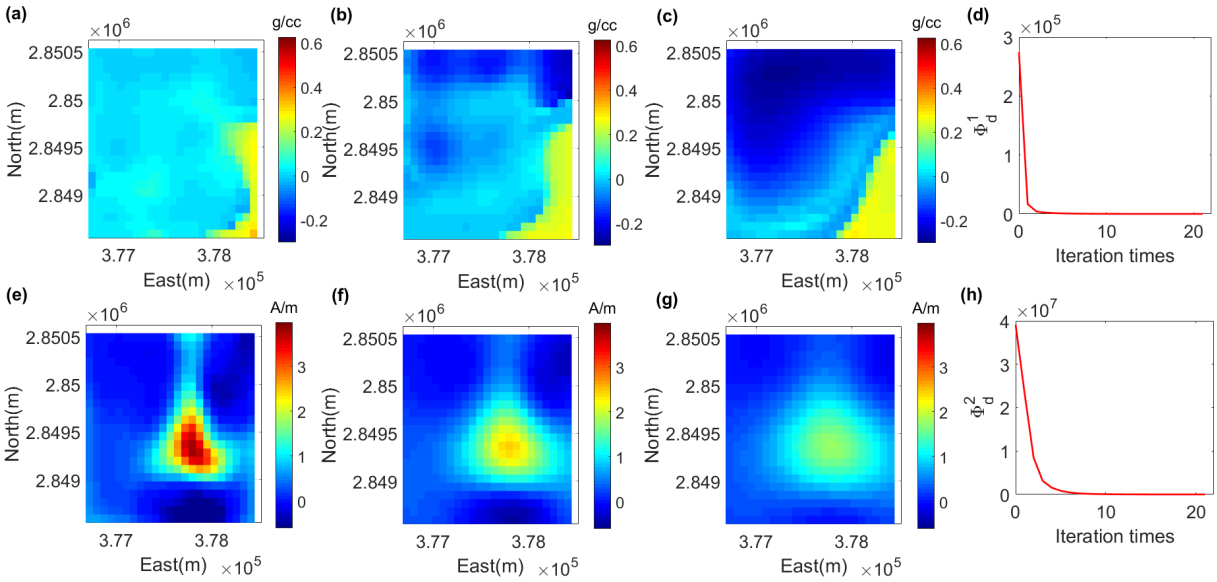

Figure 18. The result of the MS-ICG joint inversion of gravity and magnetic data. The slices of the recovered density model at z = 250 m (a), z = 450 m (b) and z = 650 m (c). (d) Convergence curve of the MS-ICG joint inversion of gravity data. The slices of the recovered magnetization model at z = 250 m (e), z = 450 m (f) and z = 650 m (g). (h) Convergence curve of the MS-ICG joint inversion of magnetic data.

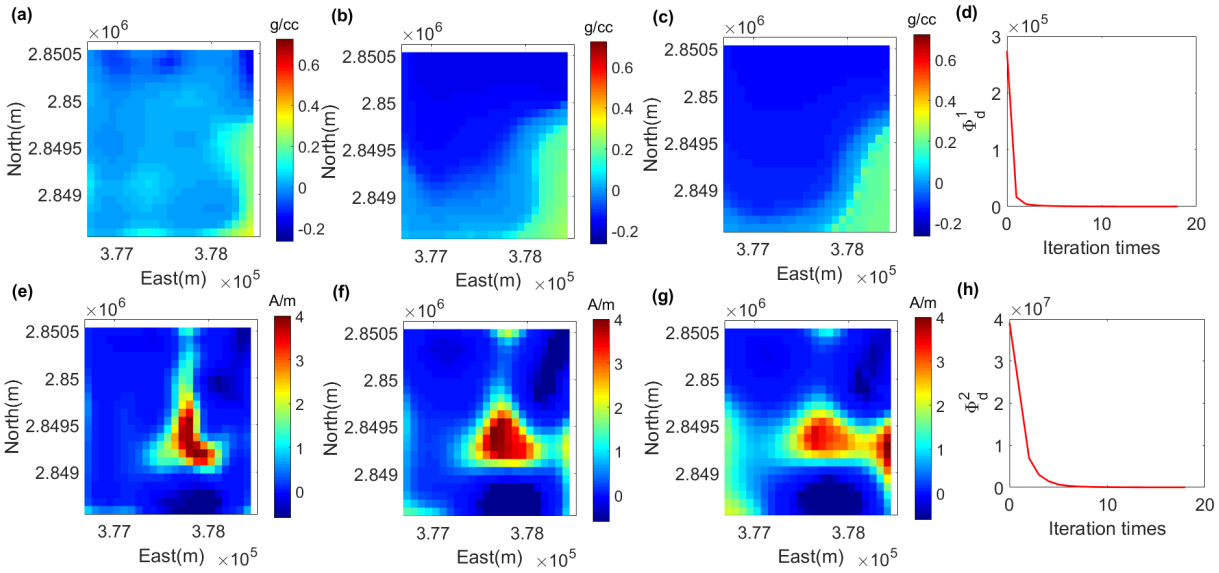

Figure 19. The result of the DS-ICG joint inversion of gravity and magnetic data. The slices of the recovered density model at z = 250 m (a), z = 450 m (b) and z = 650 m (c). (d) Convergence curve of the DS-ICG joint inversion of gravity data. The slices of the recovered magnetization model at z = 250 m (e), z = 450 m (f) and z = 650 m (g). (h) Convergence curve of the DS-ICG joint inversion of magnetic data.

sides of the working area. The recovered models of the MS-ICG joint inversion are scattered and fuzzy, while the recovered models of the DS-ICG joint inversion in the DS are focused. Furthermore, the boundaries between the geology anomalous bodies and surrounding rocks from the DS-ICG join inversion are more obvious. Additionally, the part of real data in Table 1 can be found that the memory resources required in the DS-ICG joint inversion is less than the memory cost required in the MS-ICG joint inversion, which also illustrates the efficiency of the extended method in this paper.

4. Conclusions

In this paper, the DS method and the ICG algorithm are extended to the correlation-analysis joint inversion. The DS-ICG joint inversion method has been applied on gravity data and magnetic data, including synthetic data and field data. The DS-ICG joint inversion method facilitates the combination of the stable function with sparse factor. The sparse-constrained regularization method can enhance the sparsity to maintain sharp boundaries of the reconstructed physical property models. Furthermore, the elastic-net regularization method can avoid over-sharpening and over-smoothing at the boundaries of the reconstructed models. Simultaneously, compared with the MS-ICG joint inversion, the DS-ICG joint inversion can reduce the dimensions of the computation equations, which can effectively reduce the requirements of computation cost, increase the calculation efficiency and improve the inversion accuracy. Additionally, the recovered models of field data show that the algorithm extended in this paper can quickly acquire the underground distributions of density and magnetization and effectively divide the boundaries between the geological anomalous bodies and the surrounding rock, which shows strong stability and practicality of the DS-ICG joint inversion method. Therefore, it can be illustrated that the DS-ICG joint inversion method is an effective technical means for the interpretation of field data.

Acknowledgments. This work has been supported by National Key Research and Development Program of China Project (2018YFC0603502). We thank the technical staff for carrying out field data in the mining area of Hunan province and the anonymous reviewers for their detailed and constructive comments that greatly contributed to the improvement of the paper. The authors would like to thank editor for his contribution to improve this paper.

References

Afnimar, K. K. and K. Nakagawa (2002). Joint inversion of refraction and gravity data for the three-dimensional topography of a sediment-basement interface, Geophys. J. Int., 151, 1, 243-254.

Bosch, M. (1999). Lithologic tomography: From plural geophysical data to lithology estimation, J. Geophys. Res., 104, B1, 749-766.

Bosch, M. Mc. and J. Gaughey (2001). Joint inversion of gravity and magnetic data under lithologic constraints, The Leading Edge, 20, 8, 877-881.

Caratori, Tontini. F., L. Cocchi and C. Carmisciano (2006). Depth-to-the-bottom optimization for magnetic data inversion: Magnetic structure of the Latium volcanic region, Italy, J. Geophys. Res.: Solid Earth, 111, B11104, doi:10.1029/2005JB004109.

Farquharson, C. G., M. R. Ash and H. G. Miller (2008). Geologically constrained gravity inversion for the Voisey's Bay ovoid deposit, The Leading Edge, 27, 1, 64-69.

Fregoso, E. and L. A. Gallardo (2009). Cross-gradients joint 3D inversion with applications to gravity and magnetic data, Geophys., 74, 4, L31-L42.

Fu, L. and S. X. Liu (2016). Joint inversion of first arrival P waves and Rayleigh waves based on cross-gradient constraint, Chinese J. Geophys. (in Chinese), 59, 12, 4464-4472.

Gallardo, L. A. and M. A. Meju (2003). Characterization of heterogeneous near-surface materials by joint 2D inversion of dc resistivity and seismic data, Geophys. Res. Lett., 30, 13.

Gallardo, L. A. and M. A. Meju (2004). Joint two-dimensional DC resistivity and seismic traveltime inversion with cross-gradients constraints, J. Geophys. Res., 109, B3, 3311-3315.

Gallardo, L. A., S. L. Fontes, M. A. Meju, M. P. Buonora and P. P. de Lugao (2012). Robust geophysical integration through structure-coupled joint inversion and multispectral fusion of seismic reflection, magnetotelluric, magnetic, and gravity images: example from Santos Basin, offshore Brazil, Geophys., 77, B237-B251.

Gao, X. H., S. Q. Xiong, Z. F. Zeng, C. C. Yu, G. B. Zhang and S. Y. Sun (2019). 3D inversion modeling of joint gravity and magnetic data based on a sinusoidal correlation constraint, Applied Geophys., 16, 4, 519-529.

Gardner, G. H. F., L. W. Gardner and A. R. Gregory (1974). Formation velocity and density-the diagnostic basics for stratigraphic traps, Geophys., 39, 6, 770-780.

Geng, M., D. Huang and Q. Yang (2014). 3D inversion of airborne gravity gradiometry data using cokriging, Geophys., 79, 4, 37-47.

Guo, L., X. Meng and L. Shi (2009). 3D correlation imaging for gravity and gravity gradiometry data, Chinese J. Geophys. (in Chinese), 52, 4, 1098-1106.

Haber, E. and D. Oldenburg (1997). Joint inversion: a structural approach: Inverse problems, 13, 63-77.

Hou, Z., D. Huang and E. Wang (2019). 3D density inversion of gravity gradieometry data with a multilevel hybrid parallel algorithm, Applied Geophys., 16, 2, 141-153.

Lelièvre, P. G. and D. W. Oldenburg (2009). A comprehensive study of including structural orientation information in geophysical inversions, Geophys. J. Int., 178, 2, 623-637.

Lelièvre, P. G., C. G. Farquharson and C. A. Hurich (2012). Joint inversion of seismic traveltimes and gravity data on unstructured grids with application to mineral exploration, Geophys., 77, 1, K1-K15.

Lines, L. R., A. K. Schultz and S. Treitel (1988). Cooperative inversion of geophysical data, Geophys., 53, 1, 8-20.

Lin, W. and M. S. Zhdanov (2018). Joint multinary inversion of gravity and magnetic data using Gramian constraints, Geophys. J. Int., 215, 3, 1540-1557.

Li, Y. and D. W. Oldenburg (2000b). Incorporating geological dip information into geophysical inversions, Geophys., 65, 1, 148-157.

Moorkamp, M., B. Heincke and M. Jegen (2011a). A framework for 3D joint inversion of MT, gravity and seismic refraction data, Geophys. J. Int., 184, 1, 477-493.

Oldenburg, D. W. and Y. Li (1999). Estimating depth of investigation in dc resistivity and IP surveys, Geophys., 64, 2, 403–416.

Pak, Y. C., T. L. Li and G. S. Kim (2017). 2D data-space cross-gradient joint inversion of MT, gravity and magnetic data, J. Applied Geophys., 143, 212–222.

Portniaguine, O. and M. S. Zhdanov (1999). Focusing geophysical inversion images, Geophys., 64, 3, 874-887.

Qin, P., D. Huang and Y. Yuan (2016). Integrated gravity and gravity gradient 3D inversion using the non-linear conjugate gradient, J. Applied Geophys., 126, 52-73.

Siripunvaraporn, W. and G. Egbert (2000). An efficient data-subspace inversion method for 2-D magnetotelluric data, Geophys., 65, 791-803.

Siripunvaraporn, W., G. Egbert, Y. Lenbury and M. Uyeshima (2005a). Three-dimensional magnetotelluric inversion: data-space method, Phys. Earth. Planet. Inter., 150, 3-14.

Sun, J. and Y. Li (2015). Multidomain petrophysically constrained inversion and geology differentiation using guided fuzzy c-means clustering, Geophys., 80, 4, ID1-ID18.

Sun, J. and Y. Li (2016). Joint inversion of multiple geophysical data using guided fuzzy c-means clustering, Geophys., 81, 3, ID37-ID57.

Tikhonov, A. N. and V. Y. Arsenin (1977). Solutions of Ill-Posed Problems, Winston, New York.

Vatankhah, S., S. Liu., R. A. Renaut, X. Hu, J. D. Hogue and M. Gharloghi (2022). An efficient alternating algorithm for the Lp-norm cross-gradient joint inversion of gravity and magnetic data using the 2-D fast Fourier transform, IEEE Trans. Geosci. Remote Sens., 60, 1-16.

Vozoff, K. and D. L. B. Jupp (1975). Joint inversion of geophysical data, Geophys. J. Int. 42, 3, 977-991.

Yin, C., S. Sun, X. Gao, Y. H. Liu and H. Chen (2018). 3D joint inversion of magnetotelluric and gravity data based on local correlation constraints, Chinese Journal of Geophysics (in Chinese), 61, 1, 358-367.

Zhang, R. Z. and T. L. Li (2019). Joint MT and gravity inversion using structural constraints: A case study from the Linjiang copper mining area, Jilin, China, Min., 9, 407.

Zhang, R. Z. and T. L. Li (2020). 2D data-space joint inversion of MT, gravity, magnetic, and seismic data with cross-gradient constraints, Geophys. Prosp., 68, 721-731.

Zhang, R. Z., T. L. Li and C. Liu (2021). Three-dimensional joint inversion of gravity and gravity gradient data based on data space and sparse constrains, Chinese J. Geophys. (In Chinese). 64, 3, 1074-1089.

Zhang, R. Z., T. L. Li, C. Liu et al (2022). 3D Joint inversion of gravity and magnetic data using data-space and truncated gauss-newton methods, IEEE Geosci. Remote Sens. Lett-, 19.

Zhdanov, M.S., A. Gribenko and G. Wilson (2012). Generalized joint inversion of multimodal geophysical data using Gramian constraints, Geophys. Res. Lett., 39, 9.

Zhdanov, M. S. and W. Lin (2017). Adaptive multinary inversion of gravity and gravity gradiometry data, Geophys., 82, 6, G101-G114.

***CORRESPONDING AUTHOR: Shuanggen JIN**,
Shanghai Astronomical Observatory, Chinese Academy of Sciences, Shanghai 200030, China;
School of Surveying and Land Information Engineering, Henan Polytechnic University, Jiaozuo 454000, China;
Zhuhai Fundan Innovation Institute, Creative Valley, Hengqin New District, Zhuhai 518057, China,
e-mail: sgjin@shao.ac.cn